# Earthquake-scaling in Stable Continental Regions: An Example From Fennoscandia

**V. L. Stevens[1]and R. A. Sloan[1]**

[1]Department of Geological Sciences, University of Cape Town, Rondebosch, Cape Town, 7700, South Africa.

**Key Points:**

- An algorithm to find densely-spaced vertical offsets in a high-resolution DEM was developed
- Offsets along fault-scarps in Fennoscandia were found to be highly variable
- Slip-to-Length ratios and inferred stress drops were found to be high

Corresponding author: Victoria Stevens, victoria.stevens@uct.ac.za

## Abstract

We develop an algorithm to measure densely-spaced vertical offsets along a scarp-like feature, and apply it to end-glacial fault-scarps (EGFs) in Fennoscandia, a stable-continental region (SCR). We find significant variability in apparent vertical offsets, and develop an equation to estimate the uncertainty ($1\sigma$) for a given average offset and number of measurements. We calculate the slip-to-length ratios for the faults, assuming their fault-scarps were formed in a single earthquake, and find that these ratios are up to ten times higher than found in rapidly deforming regions, which have been more studied. We find potential magnitudes of the earthquakes that formed these scarps were $M_w$7-8.2. We suggest that slip-variability along ruptures could be higher than often assumed, which means paleoseismological results should have larger uncertainty, but reduces in a predictable way with increase in number of measurements, and at least 5 measurements should be taken. We also suggest that the slip-to-length ratio used to simulate earthquakes in SCRs should be $7.5\pm2\times10^{-5}$, in comparison with the Wells and Coppersmith value of roughly $2\pm 0.5\times10^{-5}$.


## 1 Introduction

Twenty-five years ago Wells and Coppersmith (WC94, Wells and Coppersmith (1994)) published a database of earthquake slip and length data which have been hugely influential in the field of seismic hazard estimation. The relationships they found, chiefly based on observations from relatively rapidly deforming faults, are still used in seismic hazard estimation across the globe, especially when studies need to estimate the size of an earthquake likely to occur on a particular fault, or estimate magnitudes from paleo-offset measurements. The WC94 relationships are still used in both plate boundary regions, more slowly deforming intraplate deformation zones and in stable continental regions.

Since that original study, a variety of earthquake rupture compilations (e.g., Leonard, 2014), and seismological estimates of earthquake stress drop (e.g., Allmann & Shearer, 2009) have suggested that the relationships derived be Wells and Coppersmith may not be the most appropriate for intraplate regions. However, Leonard (2014) relied on a small dataset of only 28 earthquakes from stable continental regions (SCRs), and it remains uncertain as to whether comparatively rapidly deforming continental collision zones (which are nevertheless generally considered to be 'intraplate') are equivalent to SCRs where

it is hypothesized that a fault may reactivate for a single large event, or at least have repeat times of hundreds of thousands of years (Calais et al., 2016).

Static stress drop (related to slip-to-length ratios in a roughly linear manner Scholz et al. (1986)) is important in seismic hazard, as it influences ground motions (e.g., Oth et al., 2017), and the relative values of stress drop in SCRs versus active regions has been debated (e.g., Allmann & Shearer, 2009; Leonard, 2014). Stress drops may be greater in SCRs due to colder, thicker lithosphere, and in many cases compositionally-controlled larger seismogenic thicknesses (e.g., Sloan et al., 2011). Longer inter-event time periods may also create frictionally stronger faults (Scholz et al., 1986). Previous work has shown that intraplate events have systematically higher stress drops than interplate events (by 2-6 times (e.g., Allmann & Shearer, 2009; Scholz et al., 1986), and we investigate that here.

The recent availability of a high-resolution LiDAR DEM covering most of Fennoscandia allows us to investigate a unique dataset of SCR earthquakes: One that is as large as any existing global dataset, but which occurs in a region of comparatively homogeneous crustal and lithospheric thickness and strain rate (Artemieva & Thybo, 2013). This uniformity of strain rate is important because intraplate and SCR faults exist on a continuum of slip-rates and earthquake repeat times, between active regions and the most stable regions (Calais et al., 2016). Due to the lack of dense GPS instrumentation, and necessarily small surface velocity signals in these regions (e.g., Kreemer et al., 2014), it is usually impossible to identify where a particular fault sits on this spectrum. Global datasets of intraplate (or even SCR) faults will be dominated by earthquakes occurring on relatively high (though still much lower than interplate structures) strain rate faults, and due to their infrequent occurrence, are mainly inferred from topography and/or geomorphology. In Fennoscandia we have a cratonic region which is undeniably a stable continental region, but where a significant number of large earthquakes, which are the focus of this study, have occurred (Lagerbäck & Sundh, 2008).

Unlike previous studies of rupture offsets that mainly focus on strike-slip faults in California (e.g., Fialko et al., 2005; Zielke et al., 2012), with offset density measurements limited to the distribution of piercing points offset by the fault rupture, the reverse scarps in Fennoscandia allow us to find offsets semi-continuously along the rupture. As offset measurement densities have increased, the variability of offsets found has also increased

(Zielke et al. (2015) and references therein). We use our offset results to analyze what this means for uncertainties in paleoseismic offset measurements, which are often propagated through to uncertainties in paleomagnitudes, and go on to influence seismic hazard estimations.

Here we develop an algorithm to find densely spaced offsets along a scarp-like feature and use it to find offsets every 2 m along 27 fault-scarps in Scandinavia (Fig. 1). We then discuss the results along with assumptions and uncertainties in our analysis.

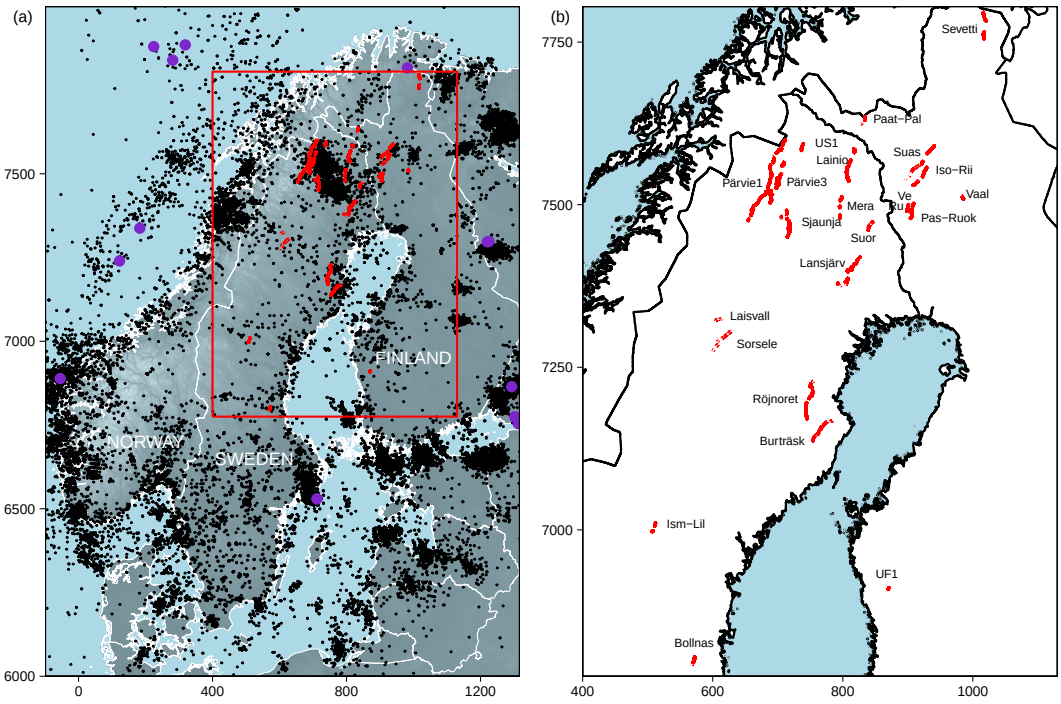


**Figure 1.** Fault locations. (a) Map of the wider region, with our study region, and (b), shown by the red box. Black dots show earthquakes from ANSS catalog, with those of $M_w \geq 5$ shown in purple. gray background shading shows the topography. This, and all subsequent map figures, are shown in UTM zone 33N, with up north, and with 1 unit on the axes roughly equal to 1 km. (b) Study region showing fault locations. Mera=Merasjaärvi, Suor=Suorsapakka, Ve=Venejärvi, Ru=Ruostejärvi, Iso-Rii=Isovaara-Riikonkumpu, Ism-Lil=Ismunden-Lillsjohogen, Vaal=Vaalajärvi, Pas-Ruok=Pasmajärvi-Ruokovaara, Paat-Pal=Paatsikkajoki-Palojärvi.

## 2 Data and Methods

### 2.1 LiDAR DEM and Fault Traces

Recent LiDAR surveys in Fennoscandia have produced DEMs with 0.6-2 m horizontal and 0.15-0.25 m vertical resolution (Johnson et al., 2015). This has allowed many more EGFs to be mapped (e.g., Mikko et al., 2015; Palmu et al., 2015; Sutinen et al., 2014). For fault-scarps in Sweden and Finland we used shapefiles provided by the Geological Survey of Sweden (based on Mikko et al. (2015)), and the Geological Survey of Finland (based on Palmu et al. (2015)) respectively. The DEMs and fault-scarp shapefiles were imported into R, which was used to extract elevation profiles perpendicular to the fault-scarp at 2 m intervals.

### 2.2 Algorithm

Several methods have previously been developed to automatically find fault-scarp offsets from high-resolution DEMs. Some of these are inapplicable as they deal with horizontal strike-slip faults and require piercing points (e.g. LaDiCaoz, Zielke et al. (2012) and 3D_Fault_Offsets, N. Stewart et al. (2018)). Two other methods which are applicable to dip-slip fault-scarps are geared towards both finding the fault, and then calculating the vertical offset, without using prior information about the location of the fault-scarp. One of these, SCARPLET (Sare & Hilley, 2018), uses landform templates to detect fault-scarps, while the other, SPARTA (Hodge et al., 2019), uses change in slope and gradient of the change in slope to detect the edges of the fault-scarp. These methods are not appropriate when the landscape contains other steep-sided, linear geomorphological features such as eskers, which can be mistakenly identified as fault-scarps.

A different, semi-automatic, more labor-intensive approach taken in Finland for a few faults (Mattila et al., 2016; Ojala et al., 2017), was to digitize the up-thrown and down-thrown edges of the fault-scarps to find the vertical difference between points along both edges of the scarp. One problem with this approach is that using the vertical difference at either edge of the fault-scarp rather than the difference between the projection of the landscape planes either side of the fault, can lead to large errors, since the original height gradient of the landscape is not taken into account.

Our method makes use of *a priori* knowledge of fault location, and relies on turning the original elevation profiles across the scarp into segmented straight-line profiles. At different steps in the algorithm, profiles are rejected and so no offset is found from that profile, if they fail to meet certain criteria (i.e. acceptable fault plane not found, acceptable landscape surfaces not found). Finally the algorithm assesses the quality of the offset measurements based on a number of parameters, as detailed below. Inputs to the algorithm are the DEM raster (a TIFF) and the fault trace (a shapefile), which here we draw on the hillshade DEM (see Fig. S1 for example hillshade DEMs). The following lists the steps in the algorithm, all of which are done in turn, automatically.

1. Extract Profiles: Elevation profiles perpendicular to the local fault-scarp orientation are extracted from the DEM every 2 m along the trace of the fault-scarp (Step 1, Fig. 2). We chose a profile half-width of 200 m. We test the sensitivity of the results to both the profile angle and the half-width. We test angles of $\pm 15°$to the perpendicular, and test half-widths of 100 m and 1000 m (see Fig. S2). Changing the angle results in a similar number of offsets found, and only a few percent difference in the average offsets found. Using a profile half-width of 100 m or 1000 m leads to more profiles being rejected (77% and 43% found respectively) than a half-width of 200 m. The average offset found is very similar for the case of 100 m but increases roughly 20% with a half-width of 1000 m, though for the fault-scarps with the largest increase, the fewest offsets were found with respect to 200 m (roughly 25%). Longer half-widths lead to fewer offsets found because there is a higher chance that non-scarp-related irregular topography is found within these profiles, which means that straight-line landscape surfaces (see Step 4) cannot be fit well.

   In cases where we see rivers cutting the faults, or the fault scarp was obviously disturbed, or in the case of the northern section of the Lainio fault, where a river channel runs parallel to the fault for some distance, we mark these on the DEM and do not attempt to find offsets in these regions.
2. Segment Profiles: For each elevation profile, 'segmented' profiles are created i.e. the profiles are simplified by approximating straight lines (Step 2, Fig. 2). This step uses the standard algorithm from the R package 'segmented' (Muggeo, 2008) - an iterative regression model with break points. We set the starting number of breakpoints (K) to 10 (though the number of breakpoints can change during the

iterations), and the maximum number of iterations to 50. Increasing K tends to increase the detail of the final 'segmented' profiles, which can lead to an increase in noise, while decreasing K often leads to oversimplification, which can smooth over the fault-scarp.

3. Find Fault Plane: A fault plane (FP) is found by selecting planes that are within 50 m either side of the marked fault trace, and have a gradient of more than three times the average gradient of the entire profile (EP), i.e. FP/EP gradient $\geq$3 (Step 3, Fig. 2). Sometimes no fault plane is found for a given profile. We tested the sensitivity of the selection criteria to different FP/EP gradient ratio values, from 1 to 10 (see Fig. S2). On average, with the strictest criteria of FP/EP gradient $\geq$10, 37% the number of planes were found compared to FP/EP gradient $\geq$3, and the average offsets found differed by 10%. If multiple potential fault planes are found, the one nearest the center is selected, given that it is not significantly smaller than the other potential fault planes. For regions where dip-slip faults are associated with topographic fronts, the FP/EP gradient criteria may need to be decreased if the slope of the fault plane is not significantly larger than that of the topographic front.
4. Find Straight-Line Landscape Surfaces on either side of the Fault Plane: If a fault plane has been identified, the algorithm tries to find straight-line landscape surfaces that fit the 'segmented' profile either side of the fault plane (Step 4, Fig. 2). The algorithm first tries the longest surface, then if it does not meet the following criteria, a shorter surface is tried, down to a minimum landscape surface length of 100 m. Surfaces are only accepted if they meet certain criteria: The difference in dip between the two landscape surfaces must be less than the average gradient of the profile; the gradient of the fault plane must be three times that of the average gradient of the surfaces; the direction of the offset found must correspond to the dip direction of the fault (i.e. if the fault is dipping down-to-the-right, the offset must conform to this); the height difference between the center of the two surfaces should not change by more than on average 2.5 m per m averaged over the last five surfaces found. This last criteria excludes an insignificant number of extreme outliers.

5. Calculate Offsets: If landscape surfaces have been found, they are extrapolated the center of the fault plane, and the vertical difference in elevation between them at this location is found (Step 5, Fig. 2).
6. Assign Confidence Values: In this stage, the algorithm assigns confidence values to the offsets found based on three criteria: 1) the maximum residual distance from the original elevations to the straight-line landscape surfaces found on each side of the fault; 2) the difference between the slope of the landscape surfaces and the fault plane; 3) the similarity of the slopes of the landscape surfaces either side of the fault plane (Step 6, Fig. 2). These criteria are chosen since 1) the smaller the distance between the landscape surfaces and the original elevations, the better the fit of the simplification. 2) The larger the difference in slopes between the fault plane and the landscape planes, the more reliably the fault is picked out. 3) The slopes on either side of the fault plane should be similar to be confident that they were originally part of the same surface. These values are then normalized and added to together to get a final confidence value between 0 and 1 for each offset measurement.
7. Remove Results with Low Confidence Values: The algorithm removes offset values if their confidence values are more than $1\sigma$ below the mean confidence value.
8. Add Overlapping Offsets: If there are overlapping fault segments, offsets from profiles on different overlapping strands are added if they are within 5 m of each other in terms of distance along the fault-scarp. This distance is measured on a smoothed single line that either follows the main fault-scarp, or runs in between two strands if they are considered to be of equal importance. On average less than 2% of the profiles are considered to overlap, with the maximum for one fault-scarp being 7% overlapping. The results show no systematic increase in offsets seen for profiles which had offsets added.
9. Smooth Offsets along Fault: As an optional last step, we then use LOESS (locally weighted scatterplot) smoothing of offsets along the fault trace. We weight the smoothing by confidence values of each offset point found, so offsets with higher confidence give more weight to the smoothing. We vary the LOESS smoothing span to highlight the variation in offsets at both the small and broad scale, as discussed further section 3.4.

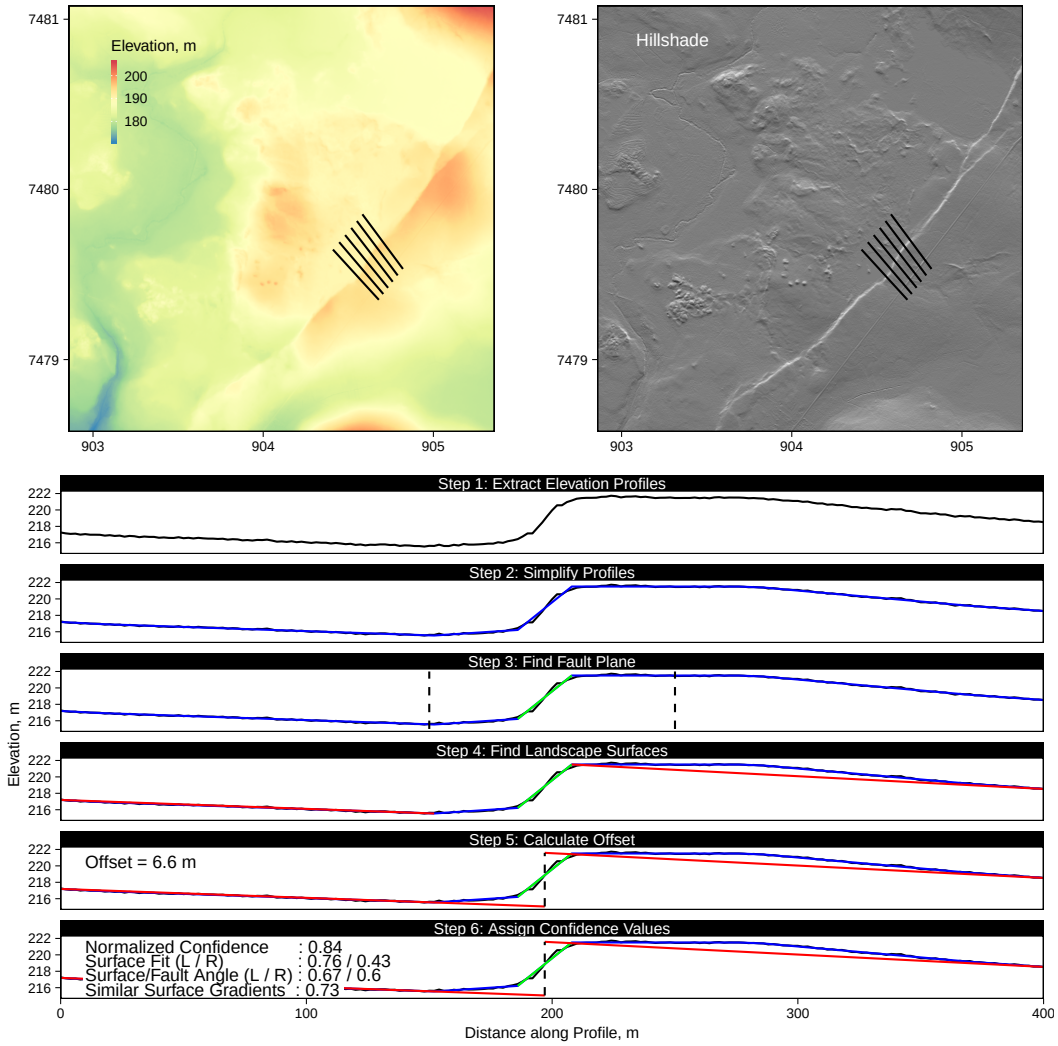


**Figure 2.** Steps in the algorithm. The upper panels show an example of a section of LiDAR DEM over the Pasmajärvi-Ruokovaara scarp. The black lines show profiles (with half-width 200 m) crossing the scarp, with angles perpendicular to the local strike of the fault-scarp. Here the lines are spaced every 50 m along the scarp for clarity, whereas in our algorithm we extracted profiles very 2 m along the scarp.

We have ignored the potential for apparent slip to be altered by the slope of the surface, which could effect the apparent vertical offset, especially if there is a lateral component of slip and/or if the slope is not perpendicular to the fault trace (Mackenzie & Elliott, 2017). Lagerbäck and Sundh (2008) note that slickensides show almost pure dip-slip motion in the few locations that they have been found, and that observations from trenches also indicate purely dip-slip reverse motion, so here we assume only dip-slip mo-

tion. In general the fault planes are very steep near the surface, though the scarp has eroded to a lower angle, and most of the faults strike parallel to the main topographic gradients in a SW-NE direction. We show this in Fig. S3, where for most of the faults, the average gradient of the landscape planes is highest when they are perpendicular to the fault.

This algorithm works for dip-slip scarps, where the trace of the scarp is known. It would work best where the topography on either side of the scarp was flat with no noise, and the fault-scarp was steep. The 'segmented' algorithm (Muggeo, 2008) is able to remove some noise, but these features must be smaller than the fault-scarp itself. The K parameter within the 'segmented' algorithm can be altered for different landscapes e.g. if the landscape were more noisy, the K value could be decreased, leading to greater simplification and better removal of noise, though fault-scarps that are not distinct would also be removed.

## 3 Results and Discussion

We found vertical offsets from studied 27 fault-scarps (Fig. 3), all steeply-dipping reverse faults thought to have formed around the time of the last deglaciation, roughly 10,000 years ago (Lagerbäck & Sundh, 2008), though there is evidence that some scarps may have formed more recently (e.g., Ojala, Mattila, Hämäläinen, & Sutinen, 2019). These EGFs have been explained by a combination of tectonic and glacial rebound stresses, possibly in combination with high-fluid pressure underneath the ice-sheets (e.g., I. S. Stewart et al., 2000). These scarps formed by reactivating older fault zones, as evidenced by wide deformation zones seen in trenches that cross the scarps (e.g., Lagerbäck & Sundh, 2008).

For five of the fault-scarps (Lansjärv, Burträsk, Sorsele, Isovaara-Riikonkumpu and Röjnoret), trenches dug across the scarps show evidence that they were formed in single events (Lagerbäck & Sundh, 2008; Ojala et al., 2017; Lagerbäck, 1992). However, for three other fault-scarps (Merasjärvi, Venejärvi and Suasselkä), there is evidence that they were formed in multiple events (Smith et al., 2018; Mattila et al., 2019; Ojala, Mattila, Ruskeeniemi, et al., 2019). The two stage origin for the Merasjärvi fault-scarp was based on geomorphology, and river terraces offset to different heights (Smith et al., 2018). A trench across the Venejärvi indicated that this may have been formed in potentially three

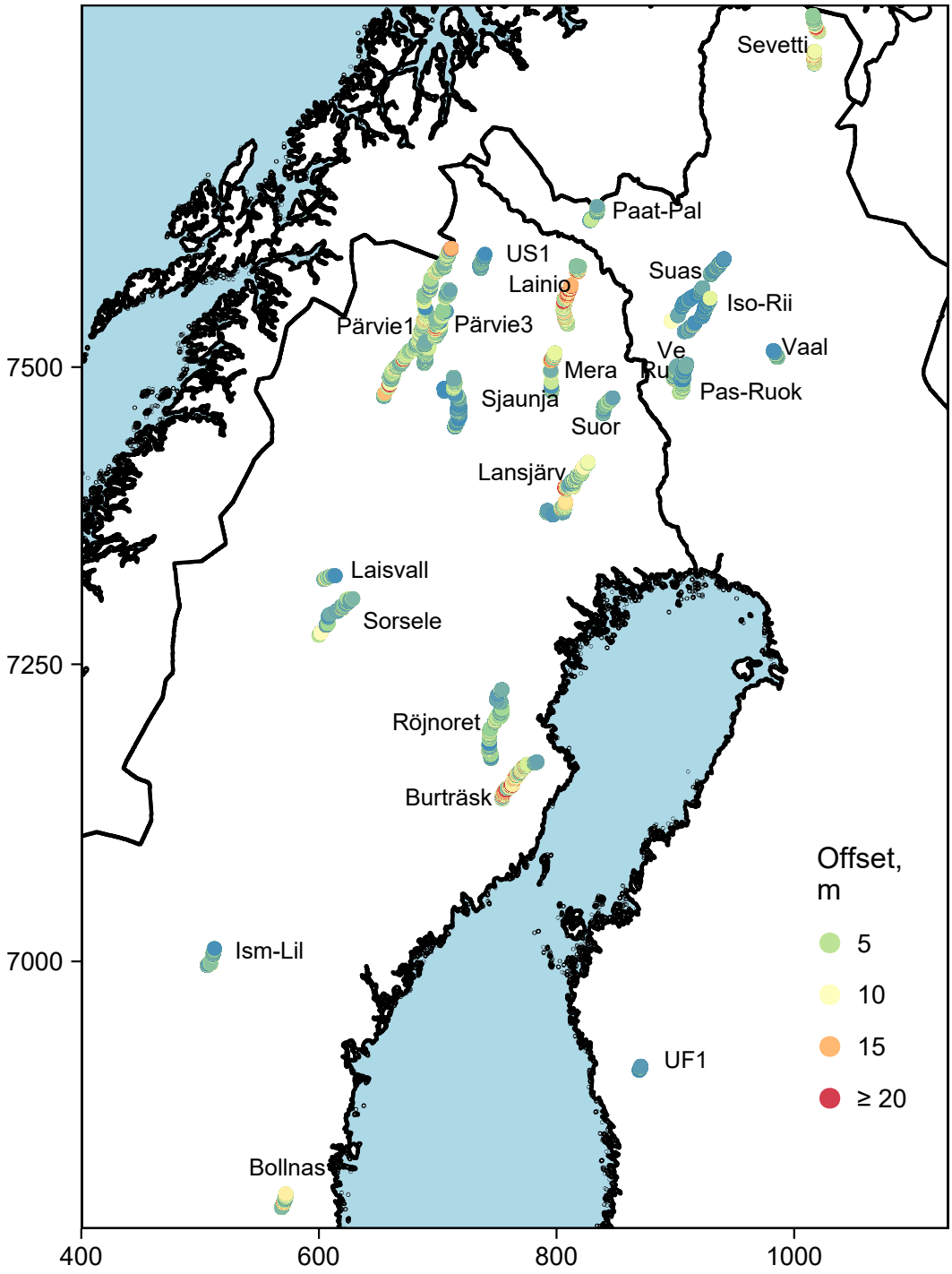


**Figure 3.** Algorithm results. Points show locations where offset measurements were found, color-coded by offset. Mera=Merasjaärvi, Suor=Suorsapakka, Ve=Venejärvi, Ru=Ruostejärvi, Iso-Rii=Isovaara-Riikonkumpu, Ism-Lil=Ismunden-Lillsjohogen, Vaal=Vaalajärvi, Pas-Ruok=Pasmajärvi-Ruokovaara, Paat-Pal=Paatsikkajoki-Palojärvi.

events, though with the third being very minor (Mattila et al., 2019). For the Merasjärvi and Suasselkä scarps, the first of the two ruptures is interpreted to have taken place prior to deglaciation, meaning that the glaciation did not fully reset the landscape.

For the Suasselk a fault, a minor strand at one site, but not the main strand, was found to indicate it formed in two ruptures, the first of which occurred prior to glaciation. At a different, and morphologically simpler, site on the same fault the main scarp is interpreted as having formed from a single postglacial rupture. (Ojala, Mattila, Ruskeeniemi, et al., 2019).

Fig. 4 shows a schematic of potential rupture scenarios in terms of single/multiple ruptures (a), and how this would influence average slip-to-length ratios found, together with an example of how this might be applied to the Merasjärvi fault-scarp (b).

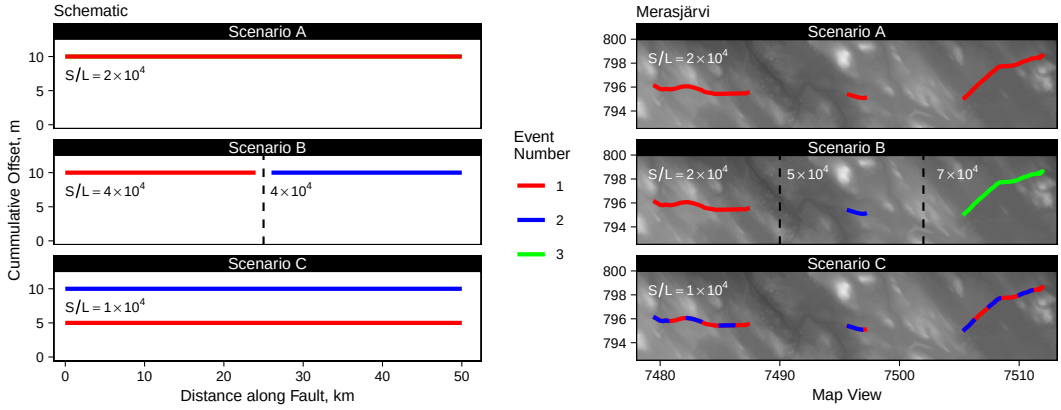


**Figure 4.** Potential rupture histories. (a) Schematic showing three rupture scenarios, A, B, and C, with the resulting slip/length (S/L) ratios that each event scenario would have. In A, the entire scarp length and offset is formed in one event. In B, first an event occurs along half of the current day scarp, and at a later stage an event occurs on the other half, with both events having the full scarp offset. In C, two events occur which both have the length of the current day scarp, but each have half the offset. (b) Three hypothetical rupture scenarios of how the Merasjärvi scarp formed. In A, the entire length and offset were formed in one event. In B, the three different segments of the scarp were formed in different events, each with their own average offset. In C, two events occurred, both along the entire length of the current scarp, though with each having half the offset.

For the fault scarps which have not been trenched, we assume they have ruptured only once, though recognize that if they were formed in multiple ruptures, their slip-to-length ratios we find here would be different. There may be physical reasons why most of the faults here only ruptured once. The earthquakes likely represent the release of strain which has accumulated over extremely long time periods, triggered by the sudden lowering of the normal stress on the fault plane. This trigger could be due to a spike in pore fluid pressure from penetration of melt-water into the crust (I. S. Stewart et al., 2000), similar to earthquakes induced by diffusion of increased pore-fluid pressure from reservoir filling (e.g., Simpson et al., 1988), or just the rapid removal of the ice load.

Indeed, Craig et al. (2016) demonstrated from modeling ice-sheet removal and isostatic rebound, that during the early Holocene, the region where the EGFs are was undergoing East-West extension with horizontal strains of up to $5\text{x}10^{-8}/yr$, apparently inconsistent with the orientation and reverse sense of motion on the fault-scarps. In this region today, GPS measurements show horizontal extension is still ongoing at rates of roughly 1 mm/yr (Kierulf et al., 2014). However, the background tectonic stress during that time, as now, was NW-SE compression from ridge-push, in agreement with the principal direction of horizontal compression from earthquake focal mechanisms outside the region of the thickest ice-sheets (Lindholm et al., 2000). Craig et al. (2016) showed that the reverse fault-scarp strikes and sense of motion are consistent with the orientation of this plate boundary forces and concluded that deglaciation acted as a trigger releasing a strain reservoir that had accumulated over Ma timescales. If this is correct it is very unlikely that a particular fault segment could have failed, been reloaded, and then failed again during the early Holocene without another trigger. This does not conflict with the possibility that for some scarps, part of the topography could be formed in a rupture previous to deglaciation (Smith et al., 2018; Ojala, Mattila, Ruskeeniemi, et al., 2019). It is however also possible that individual scarps could be formed by multiple earthquakes migrating laterally along the scarp, with the potential for some overlap that would mean the full scarp height may have been created by two ruptures in these overlapping locations. Here we assume that the offsets were all formed in single events.

The percentage of profiles where reliable offsets were found varies from 33 to 68% for the individual fault-scarps. Here we show the results of the algorithm for the Burträsk fault-scarp in Fig. 5, both with offsets in map view overlying Quaternary cover, and longitudinal profiles of distance along the fault versus offset. For detailed discussion and

figures for all the faults, see the Supplementary Information (Figs. S4-S30). Quaternary cover was downloaded from the Swedish Geodata portal and Geological Survey of Finland (see Acknowledgments for details), who mapped it from a combination of field and remote approaches.

For the Burträsk fault-scarp is roughly 20 km long, and well preserved on the surface apart from locations where it crosses lakes. We find offsets varying from a few meters up to a maximum of 28.3 m, with an average of 9.7 m. It has previously been described by Lagerbäck and Sundh (2008) as having an offset of 5-10 m, locally reaching 15 m high. Large variations over short distances can be seen in the Burträsk scarp offset, particularly near the center, where there is a 10 m vertical change over 500 m, and this also occurs in many of the other faults. A trench dug across this fault (Point A in Fig. 5) did not reach bedrock, but showed evidence that this scarp formed postglacially, with no evidence for multiple ruptures.

The maximum individual offset found was 48 m, on the Pärvie1 fault, slightly higher than previous estimates of around 40 m (e.g., Olesen et al., 2004; Lagerbäck & Sundh, 2008). The original elevation profiles, faults and landscape planes, and offsets found from the elevation profiles for the Pärvie1 fault both equally spaced along the fault, adjacent to the maximum offset profile and 1 km surrounding the maximum offset profile can be seen in Figs. S31, S32 and S33.

### 3.1 Variability of Surface Offset

All of the faults showed high short-wavelength variability in offset e.g. averaged over 100 m, 10% of neighboring values have offset differences of more than 3 m, and 1% have differences of more than 7.5 m. Variation in offset can give information on the process of dynamic rupture (e.g., Liu-Zeng et al., 2005), has implications as to how paleoseismic slip measurements should be treated (e.g., Hecker et al., 2013) and can influence seismic hazard analyses (e.g., Faure Walker et al., 2019). However, there is no agreement over how much short-wavelength slip variability at the surface is reflected in the rupture process at depth: measurement uncertainty, fault geometry, fault segmentation at depth, heterogeneity of Quaternary cover and erosion, and off-fault deformation, all have the potential to increase surface slip variability measured compared to that at depth (e.g., Gold et al., 2013; Rockwell & Klinger, 2013; Milliner et al., 2015).

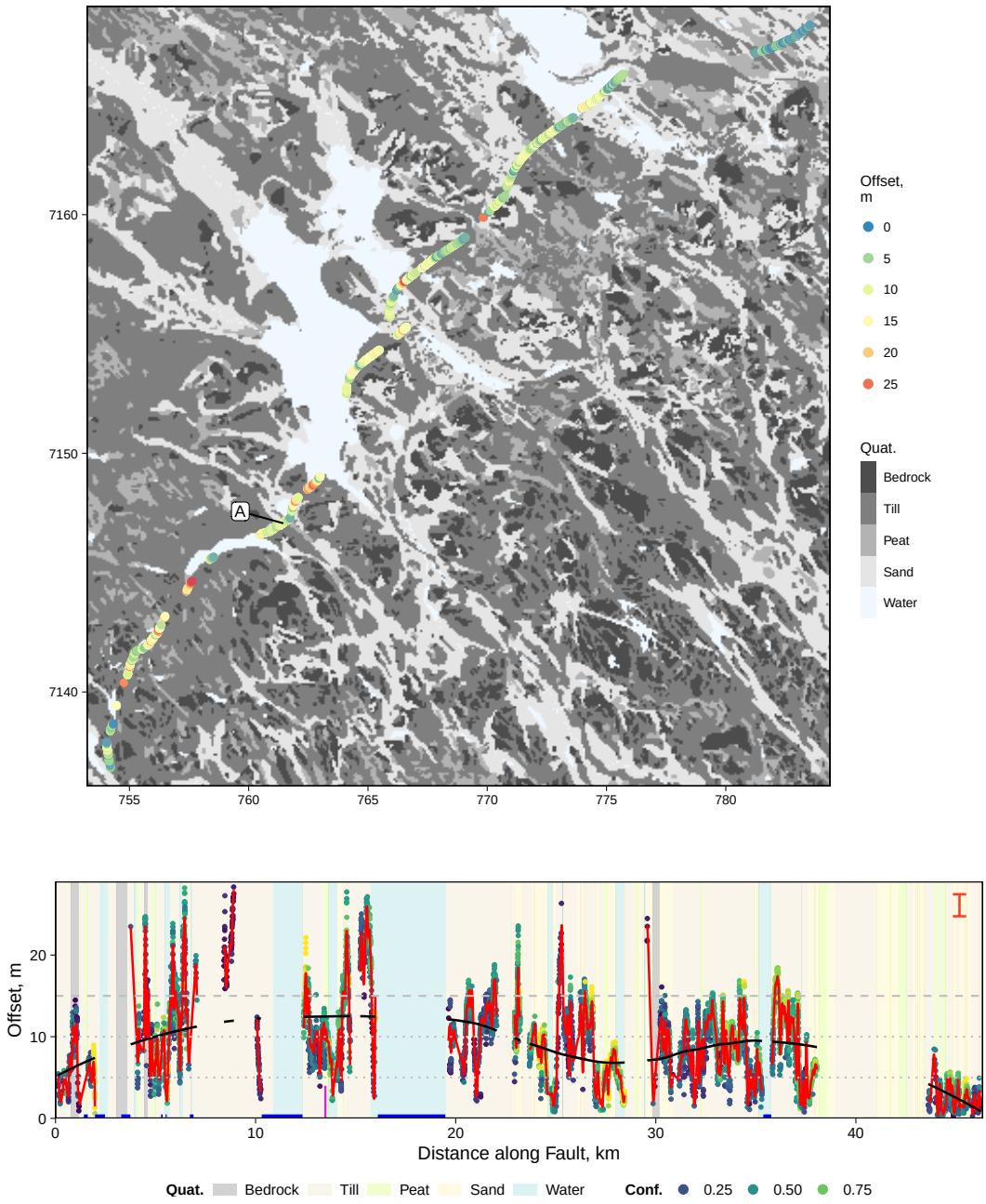


**Figure 5.** Results for the Burträsk fault scarp. The top plot shows vertical offset found on the scarp in map view and lower plot shows offset along the scarp starting from the southern end. Red and black solid line are results of locally weighted smoothing (LOESS) based on a narrower and larger smoothing window respectively. Red error bar in top right indicates the average standard deviation of measurements within the same window as the solid red line. Sections of blue lines at zero offset show where the fault-scarp could be seen but was disturbed, mainly by streams, based on the DEM. Offset points are color-coded by confidence values (Conf.) - see text for details. Quat. = Quaternary cover. A marks the location of a trench, the dotted and dashed gray lines show respectively, the average and maximum offsets found previously (Lagerbäck & Sundh, 2008).

High-offset variability has been reported in recent large strike slip events (e.g., Wesnousky, 2008; Rockwell & Klinger, 2013; Klinger et al., 2005) including variations of 1 m over tens of meters with strains of $\sim 10^{-1}$ for the Landers $M_w$7.3 1992 event (McGill & Rubin, 2002) and variations of 3 m within 10-100 m for the $M_w$7.1 1999 Hector Mine earthquake (Chen et al., 2015).

DEM accuracy also has an influence. The DEM has an average vertical accuracy of 0.15-0.25 m, so the offset change between two profiles could have an uncertainty of up to 0.5 m. This could explain some of the short wavelength (<5 m) variability.

We show in Fig. S3 that on average, the topographic slope direction is nearly perpendicular to the fault-scarps, so the vertical offsets found here are unlikely to be significantly influenced by pre-existing landform geometry (e.g., Mackenzie & Elliott, 2017). However, influences from localized changes of strike can be seen for the Lansjärv fault (Point A Fig. S12) where offset increases from 5-10 m to 20-25 m over 2 km when making a 270° box-corner bend, and some geometrical complexity may be the cause of the very large offsets seen for the Lainio fault (Point A Fig. S8) where a short scarp 1.5 km in front of the main scarp has offsets 25-30 m, and the main scarp either side offsets of roughly 10 m. Some variability may relate to real segmentation of the fault at depth (Wesnousky, 2008).

Quaternary cover also influences offsets (Figs. S37, S38 and S39) e.g. sand and peat are more likely to build up on the down-thrown side and are more susceptible to erosion, so we see lower offsets in these regions, whereas the scarp in till is better preserved. This is particularly noticeable for the Venejärvi, Pasmajärvi-Ruokovaara, Bollnas. Till makes up 80% of the profiles, and peat 15%, with the remaining 5% split between bedrock, sand and water.

Occasionally planes are found where the scarp has been significantly eroded, though these are likely to have a lower confidence value, and where the erosion stops, the offset found may increase rapidly. Roughly 6% of strain values between neighboring profiles were more than 1 (i.e. >2 m vertical offset difference over 2 m horizontally). This is hard to explain by anything other than post-earthquake landscape modification, such as small-scale geomorphic processes, since strains of this level have not been seen from fault-scarps studied within a few months after their formation (e.g., Klinger et al., 2005).

When averaged into 10 m bins, no adjacent 10 m bin average had a strain of over 1 (see Fig. S40).

The amount of off-fault deformation is extremely hard to quantify for paleoseismic scarps, and can be influenced by the Quaternary cover and thickness (e.g., Quigley et al., 2012). The importance of off-fault deformation is unclear, with recent studies finding both little (e.g., Klinger et al., 2006; Oskin et al., 2012) or up to 100% of the total displacement takes place off-fault (Milliner et al. (2015) and references therein). Nissen et al. (2014) used LiDAR differencing across a few hundred meters, not just the fault itself, and found a smoother profile, suggesting some variability occurs at shallow depths.

#### *3.1.1 Average surface offset standard deviation*

We analyze how the number of measurements taken along the scarp changes the standard deviation of the average offset found (Figs. 6, S41, S42 and S43). This is important in paleoseismology as the average offset and its uncertainties affects calculated magnitudes, which are then used in seismic hazard analyses. We randomly sample the distribution of offsets for each fault a different number of times before averaging, to model taking a different number of measurements in the field then averaging. We do this 1000 times, then calculate the standard deviation of the averages found.

From least-squares regression, fitting all the faults simultaneously, we find that

$$log(sd) = C_1 \times log(num\_meas) + C_2 \times av\_slip \quad (1)$$

where $C_1 = -0.515$ and $C_2 = 0.19$, $sd$ is the standard deviation of the average offset, $num\_meas$ is number of measurements taken and $av\_slip$ is the average slip found in meters. The fit is shown by black lines in Fig. 6 (b), while the number of measurements that need to be averaged to get within 10 and 25% are shown in Fig. 6 (c) and (d). For some scarps more than 25 observations are needed to reach a 50% probability of calculating an average offset within 10% of that of the whole dataset. This suggests that variability in scarp height poses a significant source of uncertainty in average offset (and so earthquake magnitude) estimation. This analysis assumes that measurements are taken at random, though in the field results are likely biased towards higher offsets.

We compare our predicted standard deviations with measurements found from previous studies for three other surface ruptures that each have more than 80 offset mea-

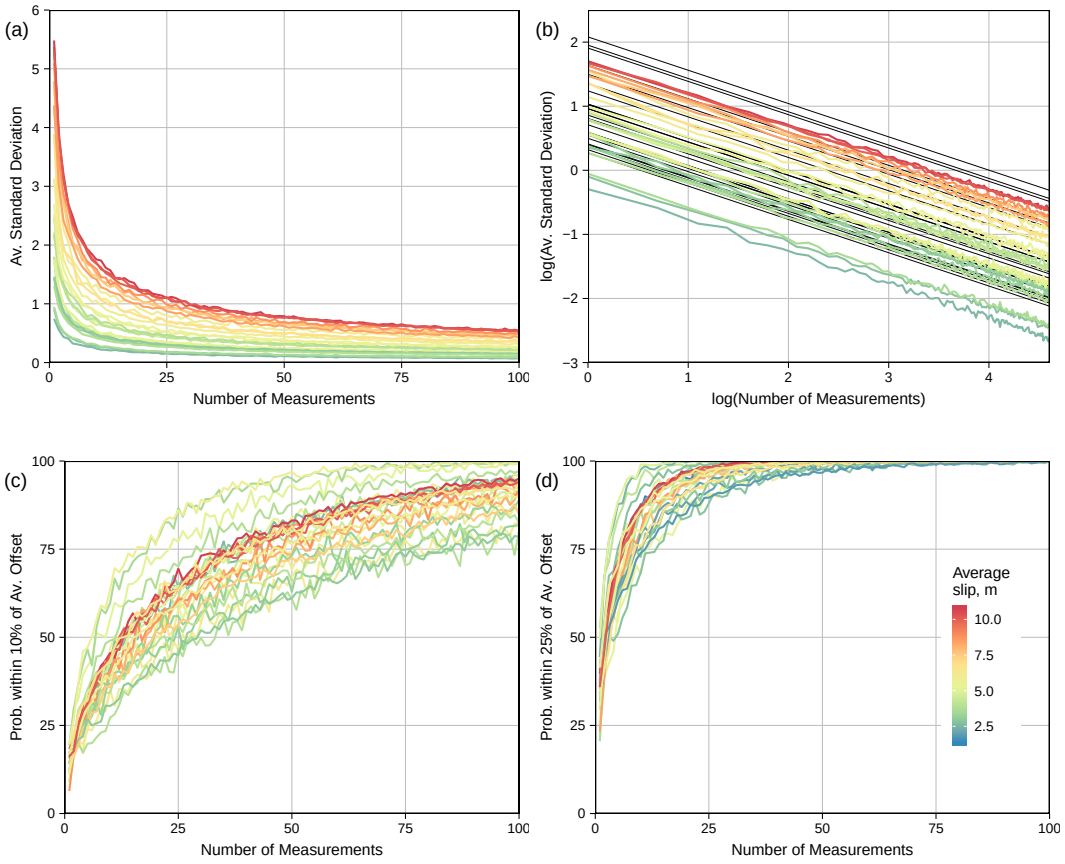


**Figure 6.** Average offset uncertainties. (a) Number of hypothetical offset measurements taken versus the average standard deviation of the average offset found. (b) Number of hypothetical offset measurements taken versus log(average standard deviation) of the average offset found. Straight black lines show the modeled fit based on equation 1. (c) The probability of the average offset found being within 10% of the actual average offset. (d) The probability of the average offset found being within 25% of the actual average offset.

surements along strike (Fig. S44). Two of these surface ruptures are strike-slip scarps formed in the instrumental period, with offsets found from reconstructing piercing points from high-resolution imagery: the 2001 $M_w$7.8 Kokoxili rupture on the Kunlun fault, and the 1999 $M_w$7.1 Hector Mine earthquake rupture (Klinger et al., 2006; Wesnousky, 2006). The third surface rupture is the paleoseismic dip-slip $M_w$ ~8 Bilila-Mtakataka fault-scarp in Malawi, where offsets were found from scarp-perpendicular elevation profiles, with manual picks of the crest and base of the scarp (Hodge et al., 2018).

For the Kokoxili and Bilila-Mtakaka fault-scarps, our predictions of standard deviation were larger than those from the measurements themselves (0.9 versus 0.6 m, and

4.9 versus 2.6 m respectively). For the Hector Mine scarp, our prediction and the standard deviation from the measurements was equal, both at 0.5 m. Since none of these measurements were automatic, there may have been bias to measuring offsets from larger, clearer faults scarps. Indeed, for the Bilila-Mtakataka, the measurements we compared with were only those found by Hodge et al. (2018) to be repeatable, which excluded in particular measurements taken towards the end of the fault-scarp. The offset measurements for the Kokoxili rupture were also taken from a central segment, which may have less variation than over the total fault length.

### 3.2 Maximum offset: 100, 95, 90th percentile

We find that the 90th and 95th percentile maximum offset are 1.7 and 2 times the average offset respectively, while the 100th percentile maximum value has little correspondence to the average offset, though does correspond more to the length of the fault (Figs. S45). The Parvie1 Fault is both the longest fault and the fault with the highest 100th percentile offset, of around 48 m (see Fig. S32 for profiles). However, this very high offset is not laterally continuous, as can be seen from Fig. S33 which shows that the highest offset extends for less than 1 km. The extreme offset values may be caused by very local features and/or the geometry of the fault, so depend on local conditions rather than general properties of the rupture such as the average offset. The extreme offset values are also more likely to be influenced by a few wrong measurements than is the average. It may be that if a fault is longer, there is simply a higher chance that an anomalous offset will be encountered, which would explain the linear relationship between absolute maximum offset and length.

Previous studies (e.g., Wells & Coppersmith, 1994; Manighetti et al., 2005; Wesnousky, 2008; Leonard, 2010) find that the maximum offset is around twice the average, though with large variation (for Wells and Coppersmith (1994) it varied from $1.25-5$, for Wesnousky (2008) it varied roughly $2-4$ for reverse faults), a wider range than the 90th or 95th percentile offsets found here, though less than the 100th percentile offset. Since the maximum offsets may occur over a short distance, in previous studies that have less dense measurements, the absolute maximum values may have been missed. If the 90th or 95th percentile values were used in these studies, the maximum:average offset ratios may have clustered more around $1.7-2$. The larger standard deviation in scaling relation that use the maximum slip rather than average slip (Wesnousky, 2008) can

be explained by the unstable nature of the 100th percentile maximum slip value. We regard the 95% value to be a more useful parameter for assessing fault scaling.

### 3.3 Rupture Length Uncertainties

The lengths of the ruptures that we see in the DEM are the minimum possible rupture length, since the rupture could continue with either a lower offset that we cannot pick up, or may have been lost through erosion. In some cases, the Quaternary cover changes e.g. from till to a material less favorable to preservation such as peat or sand, and so the fault trace appears to stop abruptly. In some cases, separately-named scarps may actually be continuations with each other, and not seen in between due to Quaternary cover unfavorable to scarp preservation. For instance, the Isovaara-Riikonkumpu scarps are separated by peat bogs (Fig. S23), and trench excavations between them have found evidence that the scarp continues beneath the ground in between (Ojala et al., 2017), so we treat this as being formed in one event. For other scarps it is not so clear - see Text S1 for more details.

For all scarps, the surface rupture could originally have extended further either side of the surface scarp still visible today, and subsequently been eroded. Since offsets along fault scarps are expected to be greatest nearer the middle and taper smoothly to zero at either end (e.g. (Wesnousky, 2008)), we can estimate how much scarp could be missing at either end by trying to fit theoretical slip-distribution profiles to the observed length-offset distributions that we have found.

#### *3.3.1 Fitting the Theoretical Slip-Distribution.*

We assume that fault slip-distribution profiles follow the sinesqrt approximation suggested by (Biasi & Weldon, 2006), which is then multiplied by an asymmetric function (Wesnousky, 2008). We also allow offsets in areas of different Quaternary cover to be shifted up or down by a constant value to account for different erosion rates in the different Quaternary types. We use fmincon (implemented in R) to minimize the absolute difference between the observed offsets ($D_{ob}$) and the theoretical offsets ($D_{th}$) calculated below:

$$D_{th}(l) = C\,[sin(\frac{\pi l}{L})]^{0.5} \times (1 - A\,(\frac{l}{L})) + Q_i \tag{2}$$

where $D_{th}$ is the theoretical offset, $C$ is a constant related to the average offset, $L$ is the rupture length, $l$ is the distance along the fault and is in the range $0-L$ and $A$ relates to how symmetric or not the distribution is. $Q_i$ is a constant that differs in regions of different Quaternary cover.

We do not initially know the length of the fault, so we set $L = L_{ob} + L_s + L_n$, and $l = l_{ob} + L_s$, where $L_{ob}$ is the observed length of the fault-scarp, $L_s$ and $L_n$ are the additional length to the south and north of the observed scarp respectively, and $l_{ob}$ is the original distance along the fault measured from the southern end of the observed fault-scarp.

**Constraints**

We constrain $C$ to be a positive number and $A$ to be between 1 and -1 (with zero being symmetric). $L_s$ and $L_n$ are constrained to be between 0 and a value determined by studying the Quaternary cover to get a best guess of how far the fault could potentially extend without being visible in the DEM i.e. if there is peat and water, the fault could easily extend through this unobserved, but if there is till and bedrock, the fault may not be able to extend through this unobserved. In some cases the parameters estimated hit this limit, so this best guess is important, whereas in other cases this limit is not reached.

$Q_i$ is set to be zero for till, since this is by far the most common Quaternary cover. $Q_i$ for bedrock is constrained to be negative (we assume that ruptures in the bedrock would erode less than till) and $Q_i$ for peat, sand and water are constrained to be positive (we assume the scarps in these areas are in general lower, as is generally seen).

We solve for $C$, $L_s$ and $L_n$, $A$ and $Q_i$, and plot the results as red lines in Figs. S46, S47 and S48.

**Assumptions**

It can be seen that for some faults (Figs. S46-S48), in particular Röjnoret, Burträsk, and Lainio, fit this distribution fairly well, though for others the validity of this fit is more questionable. Fig. 7 looks at fitting the slip-distribution for the Lainio and Merasjärvi scarps both separately and together. In this case, the scarps are fit better by assuming they were formed individually, and not in the same event. The slip-distributions for some of the other scarps (e.g. the Lansjärv scarp, Fig. S47) could also be fit equally well, or

better, if they were broken into smaller segments, so in these cases we cannot use the fit to the modeled slip-distribution as evidence that the scarp formed in a single event. We assumed a tapering scrap, and we have not allowed for segmentation, or abrupt terminations which both do occur (e.g., Hemphill-Haley, 1999; Manighetti et al., 2005; Wesnousky, 2006; Biasi & Wesnousky, 2016), and would cause non-smooth offset distributions. There are also other theoretical slip-distributions such as triangular, tapered etc. that we have not considered here (Wesnousky, 2008; Biasi & Weldon, 2006).

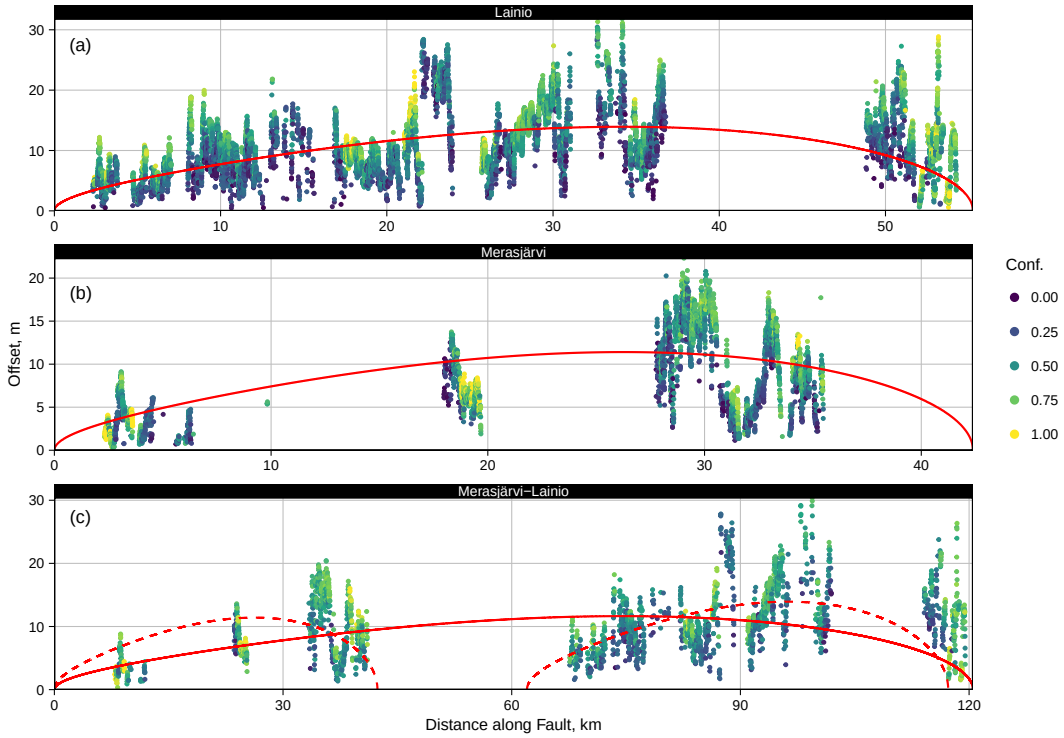


**Figure 7.** Example of fitting theoretical slip-distributions to the offsets found here for the Lainio and Merasjärvi scarps. In a) and b), the Lainio and Merasjärvi scarps are fitted separately. In c), the Merasjärvi-Lainio scarp is fitted together as one fault. Solid red lines show the theoretical slip distributions. The dashed red lines in c) show the individually fitted curves for comparison.

### 3.4 Slip-to-Length Ratios

To find the slip from the vertical offset we need the dip of the faults at the surface. In occasional bedrock scarps, dips of up to 85° have been recorded (Muir-Wood, 1993), though seismic reflection profiles and microseismicity patterns show faults dipping ∼40-

60° at depth (Lagerbäck & Sundh, 2008). Here we simply assume that the vertical offset equals the total slip on the fault. For dips of 60 to 85°, the slip would increase by ∼15 to ∼0%, and the ratios would increase correspondingly.

How to calculate the 'average' slip from an slip profile is subject to interpretation. Using a straight average can increase the influence of locations that have been eroded to lower offsets, however fitting an envelope can increase average displacement by ∼15% (Biasi et al., 2013), and increases the importance of local maxima which may be outliers (Gold et al., 2013).

Here we use the average from LOESS (locally weighted scatterplot) smoothing with a span of 250 m, weighted by confidence values, since this decreases the importance of some extreme values, while not ignoring them completely. This changes the values from straight averaging by up to 25% for an extreme case, though for more than half the profiles it changes by less than 3%. The surface expression of parts of some of the fault-scarps have been erased by later surface modification. Lengths found from the algorithm are therefore lower bounds. We fit the modeled theoretical slip-distribution (Section 3.3.1) to the profiles to estimate an amount of missing length.

The offsets on some faults (e.g. Burträsk, Röjnoret, Lainio) fit the theoretical distribution well (see Figs. S46, S47 and S48). On average, this fit makes the faults 33% longer, though for the well-fitting faults mentioned above this number is 10% (Fig. S49). We consider here only the surface rupture length and average surface slip, without considering the subsurface rupture length or average subsurface slip. WC94 (Wells & Coppersmith, 1994) find that surface rupture lengths on are average 75% of the subsurface rupture lengths, and that subsurface slip is somewhere between the average and maximum surface slip. Since both subsurface length and average offset might be larger than surface values, the ratio between the two should be less affected. We do not considered this further.

We show fault length versus average slip in Fig. 8a). Red dots show length and slip measured from the algorithm, which we consider an upper bound for the slip-to-length ratio, and the red lines extend to the length and average slip of the modeled theoretical slip-distribution profiles, which we consider a lower bound.

The darker red shaded area shows the least-squares fit the data from the observed and theoretical ratios: $9\pm2.2\times10^{-5}$ and $6\pm1.6\times10^{-5}$. The lighter red shading covers the ratios between the Burträsk and Suasselkä faults, which were both considered to be reliable (the Burträsk fault has been trenched, and the Suasselkä fault has been widely studied, with ratios of $2\times10^{-4}$ and $3\times10^{-5}$ respectively. The average and maximum offsets, along with lengths and ratios, can be seen in Table S1. If scarps formed through the lateral migration of multiple events then the slip would be unchanged, but the length that failed in individual events would be shorter. We are thus unable to preclude even higher slip-to-length ratios. Even after our proposed theoretical slip-distribution fit we could still be underestimating the length for some faults. If we were to assume a slip-to-length ratio of $1\times10^{-4}$, and the average offset is that found by the algorithm, the percentage of scarp length missing would be 50% for Buträsk, 90% for Sevetti, 75% for Bollnas and 80% for Laisvall. In some cases e.g. Merasjärvi and Lainio, we cannot preclude that they formed in the same event, since they are separated by peat - a material that does not preserve the scarps that well - and they have a similar strike and offsets. We therefore show both the results of assuming they ruptured individually and together, and link them with a gray dashed line.

We also plot previously proposed slip-to-length ratios, some of which include faults in any tectonic setting (e.g. WC94, Wells and Coppersmith (1994)) and some specific to stable continental regions (e.g. LE14, Leonard (2014)). Some of our results fall within the bounds for these previous results, though quite a lot have a higher slip-to-length ratio than expected. The slip-to-length ratio for the Burträsk fault is $2\times10^{-4}$, roughly ten times the average value from the Wells and Coppersmith (1994) compilation. The upper bound of $10^{-4}$ from a global compilation by Scholz (2002) lies close to our least-squares fit for this dataset. Other earthquakes in SCR regions (marked on Fig. 8a) have been found with even higher ratios e.g. $3\text{x}10^{-4}$ in the 2001 $M_w$7.6 Bhuj earthquake (Copley et al., 2011) and $2.2\text{x}10^{-4}$ in the 1897 $M_w$8 Assam earthquake (Bilham & England, 2001). Additionally, regions that are arguably less stable, but still with relatively low slip-rates, have also experienced earthquakes with large slip-to-length ratios, as shown by the Bilila-Mtakataka fault-scarp in the southern East African Rift with a ratio of $1\text{x}10^{-4}$ (Jackson & Blenkinsop, 1997), and various fault-scarps in the Lake Baikal region with ratios of up to $1.4\text{x}10^{-4}$ (Smekalin et al., 2010). In another more active tectonic setting, the 1855

Wairarapa New Zealand strike-slip earthquake also had a very large ratio of 1x10$^{-4}$ (Rodgers & Little, 2006).

Fennoscandia is part of the Fennoscandian Shield and microseismicity suggests that the seismogenic thickness is ∼40 km (Artemieva & Thybo, 2013; Lindblom et al., 2015), and that the crust is relatively cool, 400-500° at the Moho (Balling, 1995). This unusually large seismogenic thickness allows increased fault width, and potentially larger normal stresses at depth. The above-mentioned earthquakes with large slip-to-length ratios also have a large seismogenic thickness, which, rather than slip rate, may be the controlling factor, as suggested previously by e.g., Jackson and Blenkinsop (1997).

It has been suggested that some of the variability in the ratios is controlled by crustal properties (e.g., Manighetti et al., 2007). In Fennoscandia, the general structure of the crust and lithosphere is similar, since the faults are not far apart. This suggests that the geometry and properties of the local fault zones may be controlling the observed variations.

#### *3.4.1 Calculating Stress Drop.*

We use equation 7 of (Shaw, 2013) (shown below) to find the stress drop from the slip, length and width of the rupture:

$$S = \frac{\Delta\sigma}{\mu} \frac{1}{\frac{7}{3L} + \frac{1}{\frac{\lambda+2\mu}{\lambda+\mu} W}} \tag{3}$$

where $\Delta\sigma$ is the average stress drop, $\mu$ is the rigidity (here 40 GPa Dziewonski and Anderson (1981)), $S$ is the average slip, $L$ is the length and $W$ is the width of the fault rupture. We use the best estimate values of these parameters found. $\frac{\lambda+2\mu}{\lambda+\mu}$ is the Lame parameter ratio, and is equivalent to $\frac{1}{(1-\frac{V_s}{V_p})^2}$, where $V_s$ and $V_p$ are the s-wave and p-wave velocities respectively, with the $\frac{V_s}{V_p}$ ratio here taken to be 1.75.

We find (for faults longer than 20 km) average stress drops of 3-29 MPa, with a mean of 14 MPa. This is roughly twice the mean value of 6 MPa found by Allmann and Shearer (2009) for intraplate areas, which includes fault with slip rates of cm/year. However, it is similar to the Bhuj 35 MPa (Copley et al., 2011) and Saguenay 16 MPa (Somerville et al., 1990) earthquakes, which are in SCRs. Anderson et al. (2017) suggest that fault scaling is influenced by slip rate, with slower slipping faults having larger stress drops,

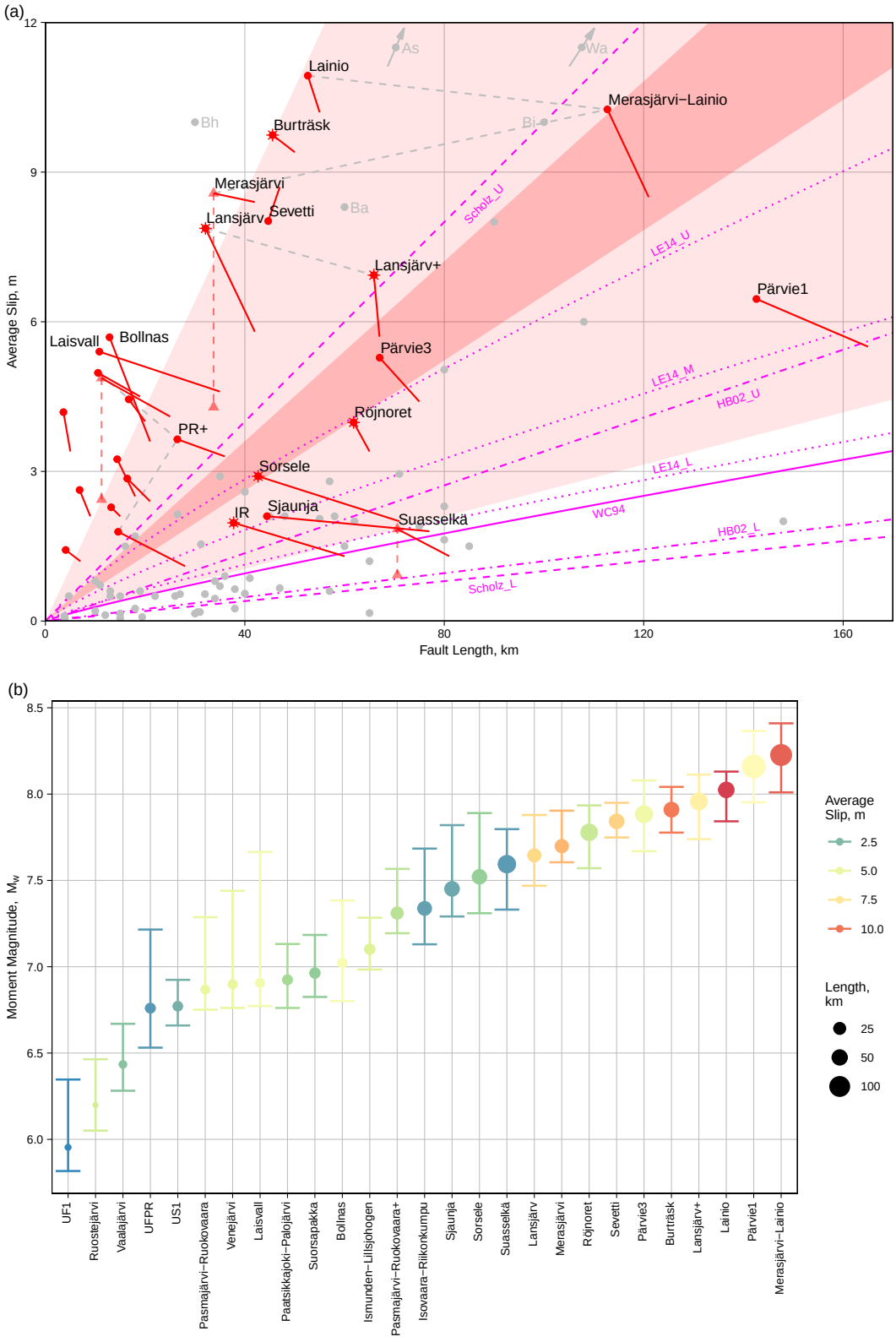


**Figure 8.** (Caption next page.)

**Figure 8.** a) Slip-to-length ratios found. Average slip versus length for faults studied. Here we take the average slip on the fault to be the same as the vertical offset, which gives a minimum slip value. If we assumed the faults were dipping 60° the slip values would all increase by 15%. Red dots show the fault length and average slip from the algorithm results. Red stars and triangles show fault-scarps that have been trenched, with evidence for single, and for multiple rupture respectively. For those with evidence of multiple ruptures, dashed red lines extend vertical to where the scarp would plot assuming the entire length was formed in two events with equal slip. Solid red lines extend to the fault length and average slip found from the modeled theoretical slip-distribution. The darker red shaded area shows the least-squares fit to the observed (upper bound) and theoretical (lower bound) ratios. The lighter red shaded area covers the ratios between the Burträsk and Suasselkä faults. gray dashed lines connect faults that may connect to each other, or extend further. gray unlabeled dots show the compilation of measurements from (Wells & Coppersmith, 1994). gray labeled dots show the Bhuj (Bh), Bilila-Mtakataka (Bi), Baikal (Ba), Assam (As) and Wairarapa (Wa) scarps mentioned in the text. The As and Wa scarp slip values lie off the plot (18 and 15.5 m respectively) so are shown as arrows at locations with the correct slip/length ratio. Pink lines show relations between slip and length found in previous papers. Scholz_U and Scholz_L are the upper and lower bound for slip to length ratio for global faults suggested by (Scholz, 2002). LE14_U,LE14_M and LE14_L are the upper, middle, and lower bounds for slip to length ratio for dip-slip faults in stable continental regions suggested by (Leonard, 2014). HB02_U and HB02_L are the upper and lower bound for slip to length ratios in continental regions suggested by (Hanks & Bakun, 2002). WC94 is the suggested slip to length relation for a global compilation of faults of all mechanisms from (Wells & Coppersmith, 1994). b) Magnitudes found. Estimated moment magnitudes with upper and lower bounds. See Fig. S50 for a GR plot of these magnitudes and Table S2 for input parameters.

potentially due to the increased healing time available between earthquakes for slower slipping faults.

### 3.5 Calculating Magnitudes.

We calculate preferred and upper and lower bounds for $M_w$ from each fault rupture, including cases where scarps could have been single ruptures, or two separate events, as shown in Fig. 8b).

We find the moment released in each event using $M_\circ = \mu LW\bar{s}$ (Hanks & Kanamori, 1979) where $M_\circ$ is the moment released, $\mu$ is the rigidity, L the length and W the width of rupture, and $\bar{s}$ is the average slip. We then find the moment magnitude from $M_w = 2/3\, log10(M_\circ) - 10.1$ (Kanamori, 1983; Aki, 1984).

The rigidity assumed here is 40±10 GPa (Dziewonski & Anderson, 1981) i.e. 30 for the lower bound, 40 for the best guess and 50 for the upper bound. For the lower bound and best guess, we use the observed lengths, while for the upper bound we use the length estimated from the theoretical slip distributions. For the lower bound we use the average offset from the theoretical slip-distributions, while for the upper bound and best guess we use the average offset found from the algorithm. We turn offset into slip assuming a surface dip of 80±10° (Muir-Wood, 1993). This may underestimate the average slip across the entire rupture plane, since many studies have found that surface slip can be several times lower than that at depth (e.g., Wells & Coppersmith, 1994; Villamor & Berryman, 2001; Fialko et al., 2005; Dolan & Haravitch, 2014) and only occasional has surface slip been found to be higher than that at depth, which may be the result of post-seismic creep (e.g., Mai & Thingbaijam, 2014). We do not take account of that here.

The width is estimated based on the length of the fault, the dip at depth (assumed here to be 50±10° based on microseismicity and seismic reflection studies, e.g. Lindblom et al. (2015); Ahmadi et al. (2015)), and the depth of the seismogenic layer (assumed here to be 40±5 km (Artemieva & Thybo, 2013; Lindblom et al., 2015)). We assume that the faults are square until their width becomes limited by the seismogenic depth, after which the width remains constant, while length continues to increase. The parameters for the magnitude calculations can be found in Table S2.

We find that the combined Merasjärvie-Lainio fault would have the largest magnitude of around $M_w 8.3^{+0.2}_{-0.3}$ if these two scarp sections ruptured simultaneously. The next largest is the Pärvie1 fault, which although longer has a lower average slip, giving a magnitude of $M_w 8.2^{+0.3}_{-0.2}$. This is similar to previous estimates e.g. $M_w$8.2±0.2 for Pärvie (Arvidsson, 1996), $M_w$±0.4 (Lindblom et al., 2015), $M_w$7.6 (I. S. Stewart et al., 2000). Current seismicity in Fennoscandia rarely exceeds $M_w$5.5 (Bungum et al., 2010) and microseismicity still clusters near EGFs (Lindblom et al., 2015). The combined moment release in all of these potential earthquakes, removing duplicate scarps, is $8^{+7}_{-4}\times10^{21}$ Nm, equivalent to about 50 years of moment build-up along the entire Himalayan front (Stevens

& Avouac, 2015), and roughly 30,000 times the moment released by earthquakes in Fennoscandia in the past 50 years. This very large moment release illustrates the large reservoir of tectonic strain that is likely to be stored in many SCR regions.

### 3.6 Implications for Paleoseismicity and Seismic Hazard Analysis

When offsets are measured, for example in paleoseismic trenches or from surface ruptures, and subsequently used to estimate magnitudes, uncertainties in the offsets need to be understood. We find that variability of offset is high, and provide an equation to estimate the standard deviation of the offset having averaged across any number of measurements. Off-fault deformation and variability of slip with depth is not accounted for, the inclusion of which could lead to higher estimated magnitudes. In addition, in the absence of dating, offsets in trenches spaced far from each other are often correlated and assumed to be formed in the same event if their offsets are similar. In a similar manner, if offsets are much higher in one trench, it is sometimes assumed that two events must have occurred here. However, if the offset variability along a scarp is high, this makes little sense.

Slip-to-length scaling relations are used widely. In paleoseismic studies, magnitudes may be calculated from scaling relations directly from the average offset found, or length may be found to then calculate the moment and magnitude. Additionally, slip-to-length scaling relations are used in probabilistic seismic hazard to create hypothetical ruptures of certain size. If the slip-to-length ratio were higher, events of the same magnitude would have a smaller rupture area with relatively higher offset. This would cause higher peak ground acceleration (PGA) over smaller areas in each event, rather than lower PGA over a wider area. We suggest that a slip-to-length ratio of $7.5\pm2\times10^{-5}$ and a stress drop of 14±9 MPa be used in SCRs. Maximum offset values should also be used with caution in scaling relations. We find that 90th or 95th percentile offsets are more stable with respect to the average offset.

The variability of offset may also have other implications for PGA; this variability may explain some of the scatter in Ground Motion Prediction Equations (GMPEs) i.e. the PGA experienced at two locations close to each other can vary greatly in the same earthquake. The distribution of earthquake moment release and frequency of seismic waves may vary widely depending on the geometric roughness of the surface ruptures and shal-

low asperities, which influence the short-wavelength offset variability (Zielke et al., 2017), and the general slip-distribution profile. If the variability in surface rupture is reflected at depth, we may be able to better model the wavelengths of seismic waves sent out from different portions of the faults.

Lastly, with respect to seismic hazard in Scandinavia itself there are two very different hypotheses that follow from recent work. Here we have suggested that during the postglacial period, very large earthquakes occurred on comparatively short faults. This does not necessarily mean that large earthquakes are likely in the future. Craig et al. (2016) suggest that deglaciation acted as a trigger releasing long-built up stresses, and that the current strain regime is actually taking north-south reverse faults away from failure. This would suggest the risk of a similar event in the near future is very low. This model is supported by previous studies which found that the scarps formed in single ruptures. However, recent work has suggested that at least some scarps are the product of compound ruptures. Here we suggested that these compound scarps may be the result of remnants of faulting prior to deglaciation being preserved through the glacial period, and then being reactivated during deglaciation. They are rare (at least where preserved in peat or till) because of the extensive erosion that occurred during that time period. In this case the likelihood of a future large earthquake is low.

Alternatively, if multiple earthquakes have commonly occurred since deglaciation, the size of individual events may be smaller, though still large, and it may be more likely that such events could reoccur. Due to the expected stress changes generated by deglaciation, and the current E-W extension observed by GNSS networks, we favor the former hypothesis (that the earthquakes are very large, with high slip-to-length ratios and the likelihood of similar events re-occurring in the area now is very low). Further detailed paleoseismic investigation is need to confirm (or refute) this hypothesis.

## 4 Conclusions

We developed an algorithm to find fault and landscape planes, and calculate vertical offsets, at an arbitrary density along the fault (here every 2 m).

We find that offset can be highly variable at the short scale and we find some faults with very high slip-to-length ratios. This may be particular to SCR regions, or to do with the specific conditions under which EGFs formed e.g. potentially high pore-fluid pres-

sure. It has been suggested that static stress drop may increase as fault slip-rate decreases, due to greater frictional healing (Anderson et al., 2017). Since slip-rates in Fennoscandia (and other SCRs) are exceptionally low, this could explain the high apparent static stress drop. Rupture variability may also depend on fault maturity. More mature faults may localize slip more, and be more likely to rupture across steps. The faults studied are generally thought to be reactivating older structures and we do not attempt to quantify their 'maturity' here.

One of the main uncertainties for some of the fault-scarps in this study was the number of events that formed these scarps. Future work to reduce this uncertainty would involve digging more trenches across these scarps, and more extensive dating to determine single/multiple origins. Further work is also needed to determine whether the unusual fault scaling characteristics found here are primarily the result of low slip rates and very long inter-event time periods, or the relatively large seismogenic thicknesses (and so normal stresses) relative to active regions, acting on the faults.

**Acknowledgments**

Shapefiles of fault-scarps in Sweden from (Mikko et al., 2015) were kindly provided by the Geological Survey of Sweden. The Swedish 2 m DEM and Quaternary cover was downloaded from the Swedish Geodata portal https://www.geodata.se/ using the GET download service. The Finnish 2 m DEM was downloaded from National Land Survey of Finland (https://tiedostopalvelu.maanmittauslaitos.fi/tp/kartta?lang=en). The Finnish 1:250,000 Quaternary cover and fault shapefiles were downloaded from the Geological Survey of Finland Hakku service (https://hakku.gtk.fi/en). The earthquakes from the ANSS catalog can be found at https://earthquake.usgs.gov/data/comcat/. The fault-scarp algorithm can be found at https://github.com/victoria4848/Fault-Scarps, DOI:10.5281/zenodo.3706429, along with more detailed instructions on usage. The vertical offset results for all the fault-scarps can be found in Dataset S1. All data for this paper is properly cited and referred to in the reference list. VLS was supported by the Claude Leon Postdoctoral Fellowship. RAS acknowledges financial support from the NRF (118831, 110780).

## References

Ahmadi, O., Juhlin, C., Ask, M., & Lund, B. (2015, jun). Revealing the deeper structure of the end-glacial Pärvie fault system in northern Sweden by seismic reflection profiling. *Solid Earth*, *6*(2), 621–632. Retrieved from `https://www.solid-earth.net/6/621/2015/www.solid-earth.net/6/621/2015/` doi: 10.5194/se-6-621-2015

Aki, K. (1984). Asperities, Barriers, Characteristic Earthquakes and Strong Motion Prediction. *J. Geophys. Res.*, *89*, 5867–5872.

Allmann, B. P., & Shearer, P. M. (2009, jan). Global variations of stress drop for moderate to large earthquakes. *J. Geophys. Res. Solid Earth*, *114*(1). Retrieved from `http://doi.wiley.com/10.1029/2008JB005821` doi: 10.1029/2008JB005821

Anderson, J. G., Biasi, G. P., & Wesnousky, S. G. (2017, dec). FaultScaling Relationships Depend on the Average FaultSlip Rate. *Bull. Seismol. Soc. Am.*, *107*(6), 2561–2577. Retrieved from `https://pubs.geoscienceworld.org/bssa/article-lookup?doi=10.1785/0120160361` doi: 10.1785/0120160361

Artemieva, I. M., & Thybo, H. (2013). EUNAseis: A seismic model for Moho and crustal structure in Europe, Greenland, and the North Atlantic region.

*Tectonophysics*, *609*, 97–153. Retrieved from http://dx.doi.org/10.1016/j.tecto.2013.08.004 doi: 10.1016/j.tecto.2013.08.004

Arvidsson, R. (1996, nov). Fennoscandian earthquakes: Whole crustal rupturing related to postglacial rebound. *Science (80-. ).*, *274*(5288), 744–746. Retrieved from http://www.sciencemag.org/cgi/doi/10.1126/science.274.5288.744 doi: 10.1126/science.274.5288.744

Balling, N. (1995, apr). Heat flow and thermal structure of the lithosphere across the Baltic Shield and northern Tornquist Zone. *Tectonophysics*, *244*(1-3), 13–50. Retrieved from https://www.sciencedirect.com/science/article/pii/004019519400215U doi: 10.1016/0040-1951(94)00215-U

Biasi, G. P., & Weldon, R. J. (2006). Estimating Surface Rupture Length and Magnitude of Paleoearthquakes from Point Measurements of Rupture Displacement. *Bull. Seismol. Soc. Am.*, *96*(5), 1612–1623. Retrieved from http://www.bssaonline.org/content/96/5/1612.abstract doi: 10.1785/0120040172

Biasi, G. P., Weldon, R. J., & Dawson, T. E. (2013). Appendix F - Distribution of Slip in Ruptures. *UCERF 3 Rep.*, 1–41. Retrieved from https://pubs.usgs.gov/of/2013/1165/pdf/ofr2013-1165{_}appendixF.pdfhttp://wgcep.org/sites/wgcep.org/files/AppendixF{_}DistributionOfSlip{_}20120709.pdf

Biasi, G. P., & Wesnousky, S. G. (2016). Steps and gaps in ground ruptures: Empirical bounds on rupture propagation. *Bull. Seismol. Soc. Am.*, *106*(3), 1110. doi: https://doi.org/10.1785/0120150175

Bilham, R., & England, P. (2001, apr). Plateau 'pop-up' in the great 1897 Assam earthquake. *Nature*, *410*(6830), 806–809. Retrieved from http://www.nature.com/articles/35071057http://dx.doi.org/10.1038/35071057 doi: 10.1038/35071057

Bungum, H., Olesen, O., Pascal, C., Gibbons, S., Lindholm, C., & VestØl, O. (2010, mar). To what extent is the present seismicity of Norway driven by post-glacial rebound? *J. Geol. Soc. London.*, *167*(2), 373–384. Retrieved from http://jgs.lyellcollection.org/lookup/doi/10.1144/0016-76492009-009http://jgs.geoscienceworld.org/content/167/2/373 doi: 10.1144/0016-76492009-009

Calais, E., Camelbeeck, T., Stein, S., Liu, M., & Craig, T. J. (2016). A new paradigm for large earthquakes in stable continental plate interiors. *Geophys. Res. Lett.*, *43*(20), 10,610–621,637. Retrieved from https://agupubs.onlinelibrary.wiley.com/doi/abs/10.1002/2016GL070815 doi: 10.1002/2016GL070815

Chen, T., Akciz, S. O., Hudnut, K. W., Zhang, D. Z., & Stock, J. M. (2015, apr). Fault-slip distribution of the 1999 Mw7.1 Hector mine earthquake, California, estimated from postearthquake airborne LiDAR data. *Bull. Seismol. Soc. Am.*, *105*(2), 776–790. Retrieved from https://pubs.geoscienceworld.org/bssa/article/105/2A/776-790/332341 doi: 10.1785/0120130108

Copley, A., Avouac, J.-P. P., Hollingsworth, J., & Leprince, S. (2011, aug). The 2001 Mw 7.6 Bhuj earthquake, low fault friction, and the crustal support of plate driving forces in India. *J. Geophys. Res. Solid Earth*, *116*(8), B08405. Retrieved from http://doi.wiley.com/10.1029/2010JB008137 doi: 10.1029/2010JB008137

Craig, T. J., Calais, E., Fleitout, L., Bollinger, L., & Scotti, O. (2016, jul). Evidence for the release of long-term tectonic strain stored in continental interiors through intraplate earthquakes. *Geophys. Res. Lett.*, *43*(13), 6826–6836. Retrieved from http://doi.wiley.com/10.1002/2016GL069359 doi: 10.1002/2016GL069359

Dolan, J. F., & Haravitch, B. D. (2014, feb). How well do surface slip measurements track slip at depth in large strike-slip earthquakes? The importance of fault structural maturity in controlling on-fault slip versus off-fault surface deformation. *Earth Planet. Sci. Lett.*, *388*, 38–47. Retrieved from http://dx.doi.org/10.1016/j.epsl.2013.11.043https://www.sciencedirect.com/science/article/pii/S0012821X13006778 doi: 10.1016/j.epsl.2013.11.043

Dziewonski, A. M., & Anderson, D. L. (1981, jun). Preliminary reference Earth model. *Phys. Earth Planet. Inter.*, *25*(4), 297–356. Retrieved from https://www.sciencedirect.com/science/article/pii/0031920181900467 doi: 10.1016/0031-9201(81)90046-7

Faure Walker, J. P., Visini, F., Roberts, G., Galasso, C., McCaffrey, K., & Mildon, Z. (2019, feb). Variable fault geometry suggests detailed fault-slip-rate

profiles and geometries are needed for fault-based probabilistic seismic hazard assessment (PSHA). *Bull. Seismol. Soc. Am.*, *109*(1), 110–123. doi: 10.1785/0120180137

Fialko, Y., Rivera, L., & Kanamori, H. (2005). Estimate of differential stress in the upper crust from variations in topography and strike along the San Andreas fault. *Geophys. J. Int.*, *160*(2), 527–532. Retrieved from http://gji.oxfordjournals.org/content/160/2/527.abstract doi: 10.1111/j.1365-246X.2004.02511.x

Gold, P. O., Oskin, M. E., Elliott, A. J., Hinojosa-Corona, A., Taylor, M. H., Kreylos, O., & Cowgill, E. (2013). Coseismic slip variation assessed from terrestrial lidar scans of the El Mayor-Cucapah surface rupture. *Earth Planet. Sci. Lett.*, *366*, 151–162. Retrieved from http://dx.doi.org/10.1016/j.epsl.2013.01.040 doi: 10.1016/j.epsl.2013.01.040

Hanks, T. C., & Bakun, W. H. (2002). A bilinear source-scaling model for M-log A observations of continental earthquakes. *Bull. Seismol. Soc. Am.*, *92*(5), 1841–1846.

Hanks, T. C., & Kanamori, H. (1979). A moment magnitude scale. *J. Geophys. Res. Solid Earth*, *84*(B5), 2348–2350. Retrieved from http://dx.doi.org/10.1029/JB084iB05p02348 doi: 10.1029/JB084iB05p02348

Hecker, S., Abrahamson, N. A., & Wooddell, K. E. (2013, apr). Variability of displacement at a point: Implications for earthquake-size distribution and rupture hazard on faults. *Bull. Seismol. Soc. Am.*, *103*(2 A), 651–674. doi: 10.1785/0120120159

Hemphill-Haley, M. A. (1999). *Multi-scaled analyses of contemporary crustal deformation of western north America* (Doctoral dissertation). Retrieved from https://elibrary.ru/item.asp?id=5353290

Hodge, M., Biggs, J., Fagereng, Å., Elliott, A., Mdala, H., & Mphepo, F. (2019, jan). A semi-automated algorithm to quantify scarp morphology (SPARTA): Application to normal faults in southern Malawi. *Solid Earth*, *10*(1), 27–57. Retrieved from https://www.solid-earth.net/10/27/2019/https://doi.org/10.5194/se-10-27-2019 doi: 10.5194/se-10-27-2019

Hodge, M., Fagereng, Biggs, J., & Mdala, H. (2018, may). Controls on Early-Rift Geometry: New Perspectives From the Bilila-Mtakataka Fault, Malawi. *Geo-*

*phys. Res. Lett.*, *45*(9), 3896–3905. Retrieved from http://doi.wiley.com/10.1029/2018GL077343 doi: 10.1029/2018GL077343

Jackson, M., & Blenkinsop, T. (1997, feb). The Bilila-Mtakataka fault in Malai: An active, 100-km long, normal fault segment in thick seismogenic crust. *Tectonics*, *16*(1), 137–150. Retrieved from http://doi.wiley.com/10.1029/96TC02494 doi: 10.1029/96TC02494

Johnson, M. D., Fredin, O., Ojala, A. E., & Peterson, G. (2015, oct). Unraveling Scandinavian geomorphology: the LiDAR revolution. *GFF*, *137*(4), 245–251. Retrieved from http://www.tandfonline.com/doi/full/10.1080/11035897.2015.1111410 doi: 10.1080/11035897.2015.1111410

Kanamori, H. (1983). Magnitude scale and quantification of earthquakes. *Tectonophysics*, *93*(3-4), 185–199. Retrieved from http://www.sciencedirect.com/science/article/pii/0040195183902731 doi: http://dx.doi.org/10.1016/0040-1951(83)90273-1

Kierulf, H. P., Steffen, H., Simpson, M. J. R., Lidberg, M., Wu, P., & Wang, H. (2014, aug). A GPS velocity field for Fennoscandia and a consistent comparison to glacial isostatic adjustment models. *J. Geophys. Res. Solid Earth*, *119*(8), 6613–6629. Retrieved from http://doi.wiley.com/10.1002/2013JB010889https://onlinelibrary.wiley.com/doi/abs/10.1002/2013JB010889 doi: 10.1002/2013JB010889

Klinger, Y., Michel, R., & King, G. C. (2006, feb). Evidence for an earthquake barrier model from Mw 7.8 Kokoxili (Tibet) earthquake slip-distribution. *Earth Planet. Sci. Lett.*, *242*(3-4), 354–364. Retrieved from https://www.sciencedirect.com/science/article/pii/S0012821X05008435 doi: 10.1016/j.epsl.2005.12.003

Klinger, Y., Xu, X., Tapponnier, P., der Woerd, J., Lasserre, C., King, G., ... King, G. (2005, oct). High-resolution satellite imagery mapping of the surface rupture and slip distribution of the Mw7.8, 14 November 2001 Kokoxili earthquake, Kunlun fault, northern Tibet, China. *Bull. Seismol. Soc. Am.*, *95*(5), 1970–1987. Retrieved from https://pubs.geoscienceworld.org/bssa/article/95/5/1970-1987/103215 doi: 10.1785/0120040233

Kreemer, C., Blewitt, G., & Klein, E. C. (2014). A geodetic plate motion and Global Strain Rate Model. *Geochemistry, Geophys. Geosystems*, *15*(10), 3849–3889.

Retrieved from http://dx.doi.org/10.1002/2014GC005407 doi: 10.1002/2014GC005407

Lagerbäck, R. (1992, mar). Dating of Late Quaternary faulting in northern Sweden. *J. Geol. Soc. London.*, *149*(2), 285–291. Retrieved from http://jgs.lyellcollection.org/lookup/doi/10.1144/gsjgs.149.2.0285 doi: 10.1144/gsjgs.149.2.0285

Lagerbäck, R., & Sundh, M. (2008). *Early Holocene faulting and paleoseismicity in northern Sweden* (Vol. 836) (No. Research Paper C 836). Geological Survey of Sweden.

Leonard, M. (2010). Earthquake fault scaling: Self-consistent relating of rupture length, width, average displacement, and moment release. *Bull. Seismol. Soc. Am.*, *100*(5A), 1971–1988.

Leonard, M. (2014, dec). Self-consistent earthquake fault-scaling relations: Update and extension to stable continental strike-slip faults. *Bull. Seismol. Soc. Am.*, *104*(6), 2953–2965. Retrieved from https://pubs.geoscienceworld.org/bssa/article/104/6/2953-2965/331932 doi: 10.1785/0120140087

Lindblom, E., Lund, B., Tryggvason, A., Uski, M., Bödvarsson, R., Juhlin, C., & Roberts, R. (2015, jun). Microearthquakes illuminate the deep structure of the endglacial Pärvie fault, northern Sweden. *Geophys. J. Int.*, *201*(3), 1704–1716. Retrieved from http://academic.oup.com/gji/article/201/3/1704/777255/Microearthquakes-illuminate-the-deep-structure-of doi: 10.1093/gji/ggv112

Lindholm, C. D., Bungum, H., Hicks, E., & Villagran, M. (2000). Crustal stress and tectonics in Norwegian regions determined from earthquake focal mechanisms. *Geol. Soc. Spec. Publ.*, *167*, 429–439. doi: 10.1144/GSL.SP.2000.167.01.17

Liu-Zeng, J., Heaton, T., & DiCaprio, C. (2005, sep). The effect of slip variability on earthquake slip-length scaling. *Geophys. J. Int.*, *162*(3), 841–849. Retrieved from http://gji.oxfordjournals.org/https://academic.oup.com/gji/article-lookup/doi/10.1111/j.1365-246X.2005.02679.x doi: 10.1111/j.1365-246X.2005.02679.x

Mackenzie, D., & Elliott, A. (2017, jun). Untangling tectonic slip from the potentially misleading effects of landform geometry. *Geosphere*, *13*(4), 1310–1328. Retrieved from https://pubs.geoscienceworld.org/geosphere/

article-lookup?doi=10.1130/GES01386.1 doi: 10.1130/GES01386.1

Mai, P. M., & Thingbaijam, K. K. S. (2014, nov). SRCMOD: An Online Database of Finite-Fault Rupture Models. *Seismol. Res. Lett.*, *85*(6), 1348–1357. Retrieved from https://pubs.geoscienceworld.org/srl/article/85/6/1348-1357/315623 doi: 10.1785/0220140077

Manighetti, I., Campillo, M., Bouley, S., & Cotton, F. (2007). Earthquake scaling, fault segmentation, and structural maturity. *Earth Planet. Sci. Lett.*, *253*(3-4), 429–438.

Manighetti, I., Campillo, M., Sammis, C., Mai, P. M., & King, G. (2005). *Evidence for self-similar, triangular slip distributions on earthquakes: Implications for earthquake and fault mechanics* (Vol. 110) (No. 5). doi: 10.1029/2004JB003174

Mattila, J., Aaltonen, I., Ojala, A. E. K., Palmu, J. P., Käpyaho, A., Lindberg, A., ... Savunen, J. (2016). Structural Geology of the Naamivittikko and Riikonkumpu postglacial fault scarps in Finnish Lapland. In *Bull. geol. soc. finl. spec. vol. abstr. 32nd nord. geol. winter meet. 13th-15th january* (p. 312).

Mattila, J., Ojala, A. E., Ruskeeniemi, T., Palmu, J. P., Aaltonen, I., Käpyaho, A., ... Sutinen, R. (2019, jul). Evidence of multiple slip events on postglacial faults in northern Fennoscandia. *Quat. Sci. Rev.*, *215*, 242–252. doi: 10.1016/j.quascirev.2019.05.022

McGill, S. F., & Rubin, C. M. (2002). Surficial slip distribution on the central Emerson fault during the June 28, 1992, Landers earthquake, California. *J. Geophys. Res. Solid Earth*, *104*(B3), 4811–4833. Retrieved from https://agupubs.onlinelibrary.wiley.com/doi/pdf/10.1029/98JB01556 doi: 10.1029/98jb01556

Mikko, H., Smith, C. A., Lund, B. B., Ask, M. V. S., & Munier, R. (2015, oct). LiDAR-derived inventory of post-glacial fault scarps in Sweden. *GFF*, *137*(4), 334–338. Retrieved from http://www.tandfonline.com/doi/full/10.1080/11035897.2015.1036360https://doi.org/10.1080/11035897.2015.1036360 doi: 10.1080/11035897.2015.1036360

Milliner, C. W., Dolan, J. F., Hollingsworth, J., Leprince, S., Ayoub, F., & Sammis, C. G. (2015, may). Quantifying near-field and off-fault deformation patterns of the 1992 Mw 7.3 Landers earthquake. *Geochemistry, Geophys. Geosys-*

*tems*, *16*(5), 1577–1598. Retrieved from http://doi.wiley.com/10.1002/2014GC005693 doi: 10.1002/2014GC005693

Muggeo, V. M. (2008). segmented: An R package to fit regression models with broken-line relationships. *R news*, *20-25*(1), 1–73. doi: http://dx.doi.org/10.1192/bjp.195.1.A6

Muir-Wood, R. (1993). *A review of the seismotectonics of Sweden (Technical report no TR-93-13).* (Tech. Rep.). EQE International Ltd.

Nissen, E., Maruyama, T., Ramon Arrowsmith, J., Elliott, J. R., Krishnan, A. K., Oskin, M. E., & Saripalli, S. (2014). Coseismic fault zone deformation revealed with differential lidar: Examples from Japanese Mw 7 intraplate earthquakes. *Earth Planet. Sci. Lett.*, *405*, 244–256. Retrieved from www.elsevier.com/locate/epsl doi: 10.1016/j.epsl.2014.08.031

Ojala, A. E., Mattila, J., Hämäläinen, J., & Sutinen, R. (2019, nov). Lake sediment evidence of paleoseismicity: Timing and spatial occurrence of late- and postglacial earthquakes in Finland. *Tectonophysics*, *771*, 228227. doi: 10.1016/j.tecto.2019.228227

Ojala, A. E., Mattila, J., Ruskeeniemi, T., Palmu, J. P., Lindberg, A., Hänninen, P., & Sutinen, R. (2017, oct). Postglacial seismic activity along the IsovaaraRiikonkumpu fault complex. *Glob. Planet. Change*, *157*, 59–72. Retrieved from https://www.sciencedirect.com/science/article/pii/S0921818117300127 doi: 10.1016/j.gloplacha.2017.08.015

Ojala, A. E., Mattila, J., Ruskeeniemi, T., Palmu, J. P., Nordbäck, N., Kuva, J., & Sutinen, R. (2019, apr). Postglacial reactivation of the Suasselkä PGF complex in SW Finnish Lapland. *Int. J. Earth Sci.*, *108*(3), 1049–1065. doi: 10.1007/s00531-019-01695-w

Olesen, O., Blikra, L. H., Braathen, A., Dehls, J. F., Olsen, L., Rise, L., ... Anda, E. (2004). Neotectonic deformation in Norway and its implications: a review. *Nor. J. Geol. Geol. Foren.*, *84*(1).

Oskin, M. E., Arrowsmith, J. R., Corona, A. H., Elliott, A. J., Fletcher, J. M., Fielding, E. J., ... Teran, O. J. (2012, feb). Near-field deformation from the El Mayor-Cucapah earthquake revealed by differential LIDAR. *Science (80-. ).*, *335*(6069), 702–705. Retrieved from http://www.ncbi.nlm.nih.gov/pubmed/22323817http://www.sciencemag.org/cgi/doi/10.1126/science.1213778

doi: 10.1126/science.1213778

Oth, A., Miyake, H., & Bindi, D. (2017, jul). On the relation of earthquake stress drop and ground motion variability. *J. Geophys. Res. Solid Earth*, *122*(7), 5474–5492. Retrieved from http://doi.wiley.com/10.1002/2017JB014026 doi: 10.1002/2017JB014026

Palmu, J.-P., Ojala, A. E. K., Ruskeeniemi, T., Sutinen, R., & Mattila, J. (2015, oct). LiDAR DEM detection and classification of postglacial faults and seismically-induced landforms in Finland: a paleoseismic database. *GFF*, *137*(4), 344–352. Retrieved from http://www.tandfonline.com/doi/full/10.1080/11035897.2015.1068370 doi: 10.1080/11035897.2015.1068370

Quigley, M., Van Dissen, R., Litchfield, N., Villamor, P., Duffy, B., Barrell, D., ... Noble, D. (2012, jan). Surface rupture during the 2010 Mw 7.1 darfield(canterbury) earthquake: Implications for fault rupture dynamics and seismic-hazard analysis. *Geology*, *40*(1), 55–58. Retrieved from https://pubs.geoscienceworld.org/geology/article/40/1/55-58/130705 doi: 10.1130/G32528.1

Rockwell, T. K., & Klinger, Y. (2013, apr). Surface rupture and slip distribution of the 1940 Imperial Valley earthquake, Imperial fault, Southern California: Implications for rupture segmentation and dynamics. *Bull. Seismol. Soc. Am.*, *103*(2 A), 629–640. Retrieved from https://pubs.geoscienceworld.org/bssa/article/103/2A/629-640/331611 doi: 10.1785/0120120192

Rodgers, D. W., & Little, T. A. (2006, dec). World's largest coseismic strike-slip offset: The 1855 rupture of the Wairarapa Fault, New Zealand, and implications for displacement/length scaling of continental earthquakes. *J. Geophys. Res. Solid Earth*, *111*(12), 1–19. Retrieved from http://doi.wiley.com/10.1029/2005JB004065 doi: 10.1029/2005JB004065

Sare, R., & Hilley, G. (2018). Scarplet: A Python package for topographic template matching and diffusion dating. *J. Open Source Softw.*, *3*(31), 1066. Retrieved from https://doi.org/10.21105/joss.01066 doi: 10.21105/joss.01066

Scholz, C. H. (2002). *The Mechanics of Earthquakes and Faulting*. Cambridge University Press. doi: 10.1017/9781316681473

Scholz, C. H., Aviles, C. A., & Wesnousky, S. G. (1986, feb). Scaling differences between large interplate and intraplate earthquakes. *Bull. Seismol. Soc. Am.*,

*76*(1), 65–70. Retrieved from https://pubs.geoscienceworld.org/ssa/bssa/article-abstract/76/1/65/118774/scaling-differences-between-large-interplate-and?redirectedFrom=fulltext

Shaw, B. E. (2013, apr). Earthquake surface slip-length data is fit by constant stress drop and is useful for seismic hazard analysis. *Bull. Seismol. Soc. Am.*, *103*(2 A), 876–893. Retrieved from https://pubs.geoscienceworld.org/bssa/article/103/2A/876-893/331735 doi: 10.1785/0120110258

Simpson, D., Leith, W., & Scholz, C. (1988). Two types of reservoir-induced seismicity. *Bull. Seism. Soc. Am*, *78*(6), 2025–2040.

Sloan, R. A., Jackson, J. A., Mckenzie, D., & Priestley, K. (2011, apr). Earthquake depth distributions in central Asia, and their relations with lithosphere thickness, shortening and extension. *Geophys. J. Int.*, *185*(1), 1–29. Retrieved from https://academic.oup.com/gji/article-lookup/doi/10.1111/j.1365-246X.2010.04882.x doi: 10.1111/j.1365-246X.2010.04882.x

Smekalin, O. P., Chipizubov, A. V., & Imaev, V. S. (2010, mar). Paleoearthquakes in the Baikal region: Methods and results of timing. *Geotectonics*, *44*(2), 158–175. doi: 10.1134/S0016852110020056

Smith, C. A., Grigull, S., & Mikko, H. (2018, oct). Geomorphic evidence of multiple surface ruptures of the Merasjärvi postglacial fault, northern Sweden. *GFF*, *140*(4), 318–322. Retrieved from https://www.tandfonline.com/doi/full/10.1080/11035897.2018.1492963 doi: 10.1080/11035897.2018.1492963

Somerville, P. G., McLaren, J. P., Saikia, C. K., & Helmberger, D. V. (1990, oct). The 25 November 1988 Saguenay, Quebec, earthquake: source parameters and the attenuation of strong ground motion. *Bull. - Seismol. Soc. Am.*, *80*(5), 1118–1143. Retrieved from https://pubs.geoscienceworld.org/ssa/bssa/article-abstract/80/5/1118/119324/the-25-november-1988-saguenay-quebec-earthquake

Stevens, V. L., & Avouac, J. P. (2015). Interseismic coupling on the main Himalayan thrust. *Geophys. Res. Lett.*, *42*(14), 5828–5837. Retrieved from http://dx.doi.org/10.1002/2015GL064845 doi: 10.1002/2015GL064845

Stewart, I. S., Sauber, J., & Rose, J. (2000, oct). Glacio-seismotectonics: ice sheets, crustal deformation and seismicity. *Quat. Sci. Rev.*, *19*(14-15), 1367–1389. Retrieved from https://www.sciencedirect.com/science/article/abs/

pii/S0277379100000949{\#}BIB78 doi: 10.1016/S0277-3791(00)00094-9

Stewart, N., Gaudemer, Y., Manighetti, I., Serreau, L., Vincendeau, A., Dominguez, S., ... Malavieille, J. (2018, jan). 3D_Fault_Offsets, a Matlab Code to Automatically Measure Lateral and Vertical Fault Offsets in Topographic Data: Application to San Andreas, Owens Valley, and Hope Faults. *J. Geophys. Res. Solid Earth*, *123*(1), 815–835. Retrieved from https://agupubs.onlinelibrary.wiley.com/doi/abs/10.1002/2017JB014863http://doi.wiley.com/10.1002/2017JB014863 doi: 10.1002/2017JB014863

Sutinen, R., Hyvönen, E., Middleton, M., & Ruskeeniemi, T. (2014, apr). Airborne LiDAR detection of postglacial faults and Pulju moraine in Palojärvi, Finnish Lapland. *Glob. Planet. Change*, *115*, 24–32. Retrieved from https://www.sciencedirect.com/science/article/pii/S092181811400024 1http://dx.doi.org/10.1016/j.gloplacha.2014.01.007http://www.sciencedirect.com/science/article/pii/S0921818114000241 doi: 10.1016/j.gloplacha.2014.01.007

Villamor, P., & Berryman, K. (2001, jun). A late Quaternary extension rate in the Taupo Volcanic Zone, New Zealand, derived from fault slip data. *New Zeal. J. Geol. Geophys.*, *44*(2), 243–269. Retrieved from http://www.tandfonline.com/doi/abs/10.1080/00288306.2001.9514937 doi: 10.1080/00288306.2001.9514937

Wells, D. L., & Coppersmith, K. J. (1994). New empirical relationships among magnitude, rupture length, rupture width, rupture area, and surface displacement. *Bull. Seismol. Soc. Am.*, *84*(4), 974–1002,A1–A4,B1–B11,C1–C49. Retrieved from http://www.bssaonline.org/content/84/4/974.abstract

Wesnousky, S. G. (2006, nov). Predicting the endpoints of earthquake ruptures. *Nature*, *444*(7117), 358–360. Retrieved from http://www.nature.com/articles/nature05275 doi: 10.1038/nature05275

Wesnousky, S. G. (2008, aug). Displacement and Geometrical Characteristics of Earthquake Surface Ruptures: Issues and Implications for Seismic-Hazard Analysis and the Process of Earthquake Rupture. *Bull. Seismol. Soc. Am.*, *98*(4), 1609–1632. Retrieved from http://www.bssaonline.org/content/98/4/1609.abstracthttps://pubs.geoscienceworld.org/bssa/article/98/4/1609-1632/350111 doi: 10.1785/0120070111

Zielke, O., Arrowsmith, J. R., Grant Ludwig, L., & Akciz, S. O. (2012, jun). High-Resolution Topography-Derived Offsets along the 1857 Fort Tejon Earthquake Rupture Trace, San Andreas Fault. *Bull. Seismol. Soc. Am.*, *102*(3), 1135–1154. Retrieved from https://pubs.geoscienceworld.org/bssa/article/102/3/1135-1154/349677 doi: 10.1785/0120110230

Zielke, O., Galis, M., & Mai, P. M. (2017, jan). Fault roughness and strength heterogeneity control earthquake size and stress drop. *Geophys. Res. Lett.*, *44*(2), 777–783. Retrieved from http://doi.wiley.com/10.1002/2016GL071700 doi: 10.1002/2016GL071700

Zielke, O., Klinger, Y., & Arrowsmith, J. R. (2015, jan). Fault slip and earthquake recurrence along strike-slip faults - Contributions of high-resolution geomorphic data. *Tectonophysics*, *638*, 43–62. Retrieved from http://dx.doi.org/10.1016/j.tecto.2014.11.004https://www.sciencedirect.com/science/article/pii/S0040195114005824

**Figure 1.**

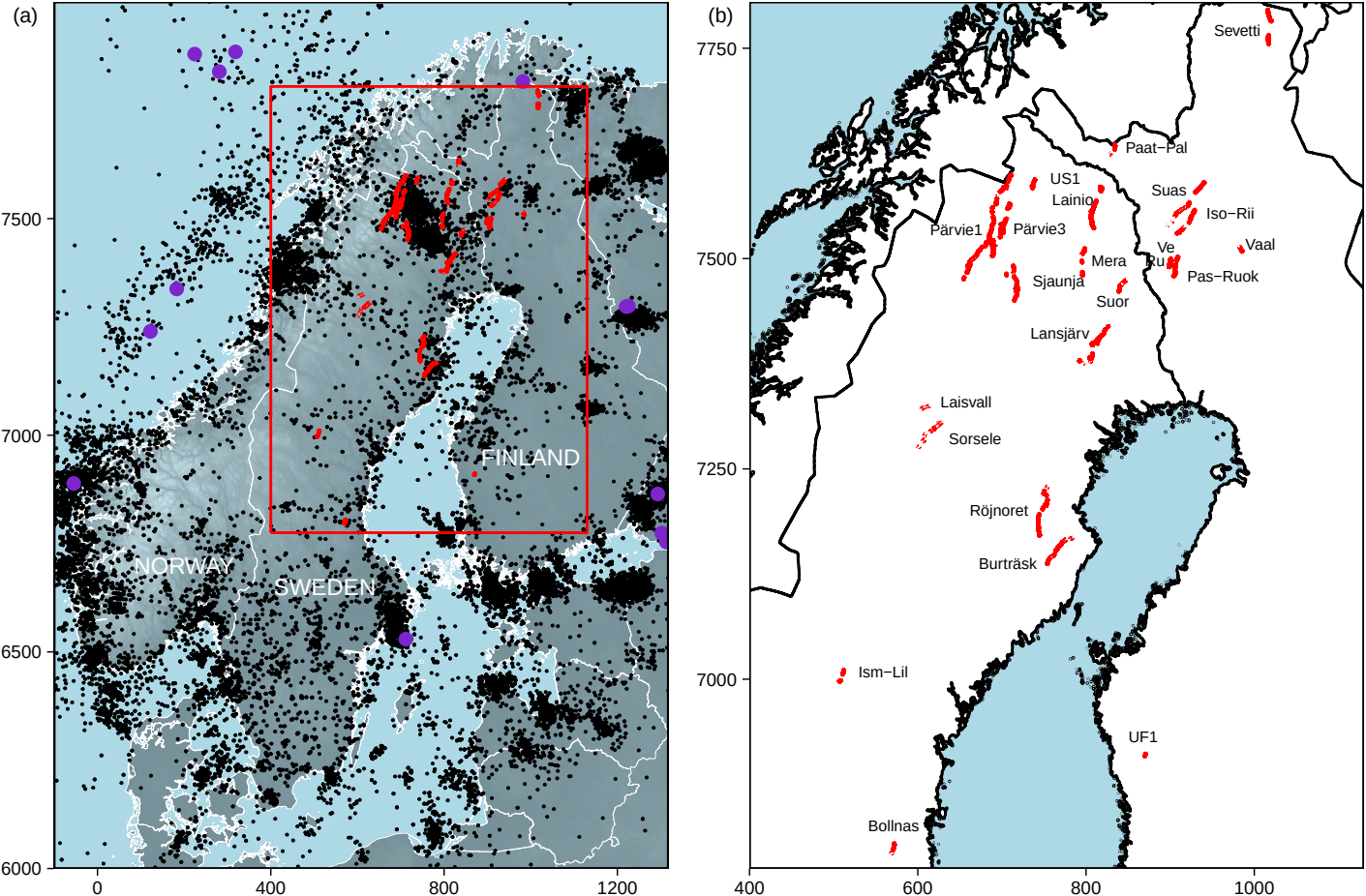
(a)
7500
7000
6500
6000
0
400
800
1200
FINLAND
NORWAY
SWEDEN
(b)
7750
7500
7250
7000
400
600
800
1000
Sevetti
Paat−Pal
US1
Lainio
Suas
Iso−Rii
Pärvie1
Pärvie3
Vaal
Ve
Ru
Mera
Sjaunja
Pas−Ruok
Suor
Lansjärv
Laisvall
Sorsele
Röjnoret
Burträsk
Ism−Lil
UF1
Bollnas

**Figure 2.**

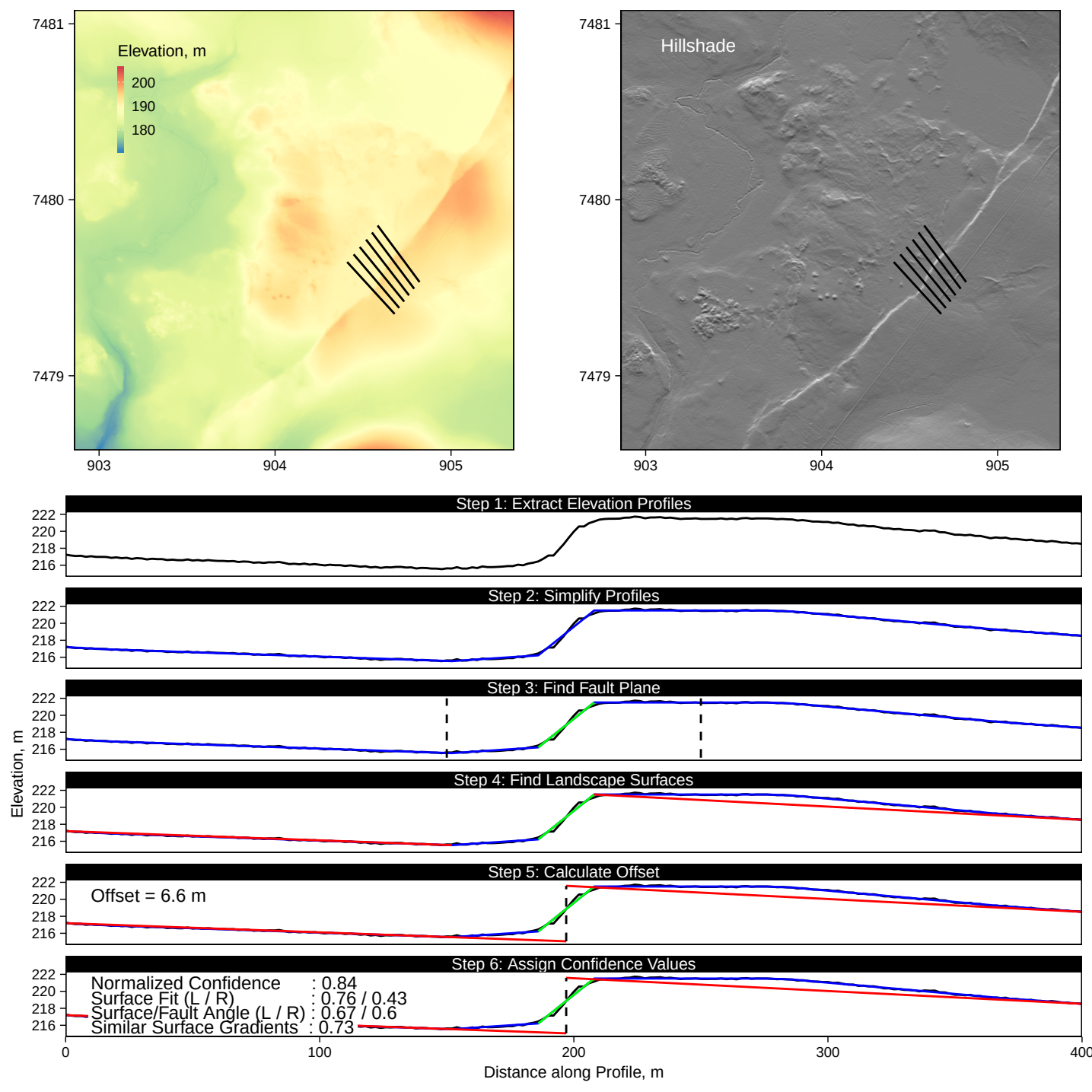
Elevation, m
200
190
180
Hillshade
7481
7480
7479
903
904
905
Step 1: Extract Elevation Profiles
Step 2: Simplify Profiles
Step 3: Find Fault Plane
Step 4: Find Landscape Surfaces
Step 5: Calculate Offset
Offset = 6.6 m
Step 6: Assign Confidence Values
Normalized Confidence : 0.84
Surface Fit (L / R) : 0.76 / 0.43
Surface/Fault Angle (L / R) : 0.67 / 0.6
Similar Surface Gradients : 0.73
222
220
218
216
Elevation, m
0
100
200
300
400
Distance along Profile, m

**Figure 3.**

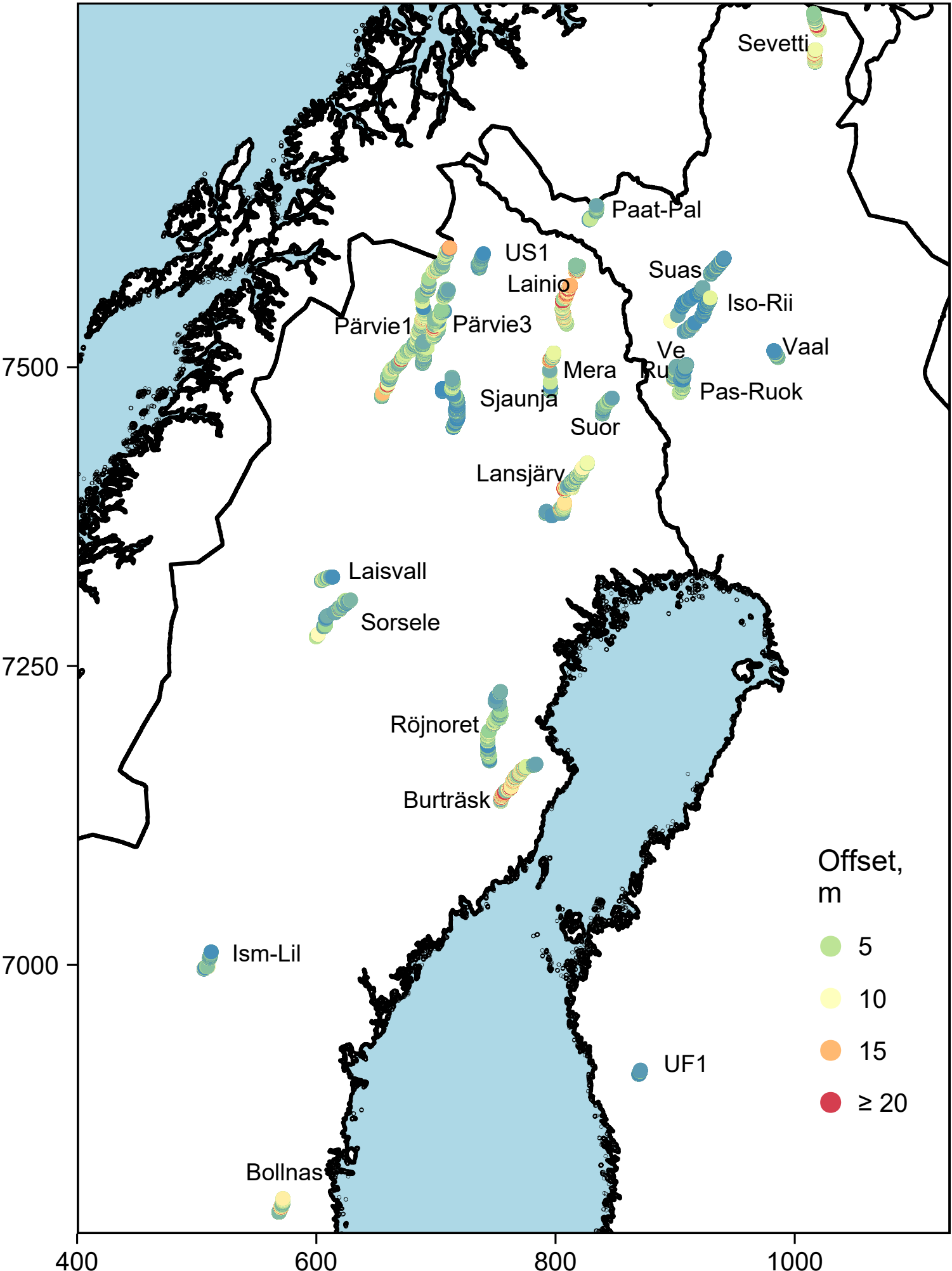
Sevetti
Paat-Pal
US1
Lainio
Suas
Iso-Rii
Pärvie1
Pärvie3
Ve
Ru
Vaal
Mera
Pas-Ruok
Sjaunja
Suor
Lansjärv
Laisvall
Sorsele
Röjnoret
Burträsk
Ism-Lil
UF1
Bollnas
Offset, m
5
10
15
≥ 20
7500
7250
7000
400
600
800
1000

**Figure 4.**

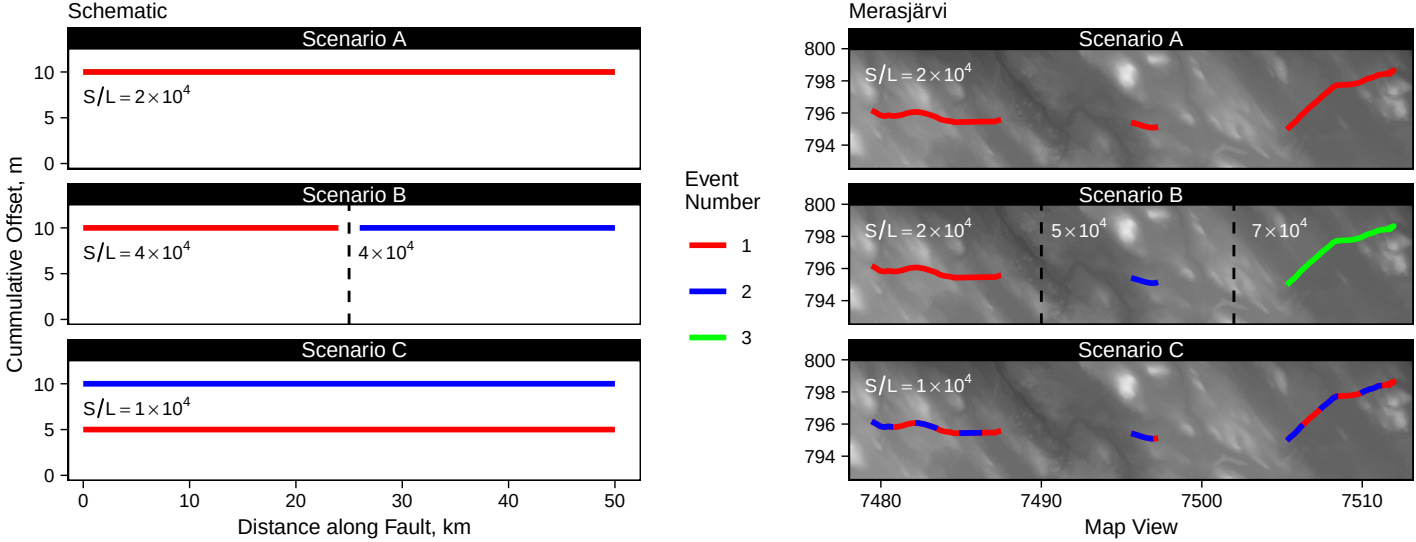
Schematic
Scenario A
S/L = 2×10^4
Scenario B
S/L = 4×10^4
4×10^4
Scenario C
S/L = 1×10^4
Cummulative Offset, m
0
5
10
Distance along Fault, km
0
10
20
30
40
50
Event Number
1
2
3
Merasjärvi
Scenario A
S/L = 2×10^4
Scenario B
S/L = 2×10^4
5×10^4
7×10^4
Scenario C
S/L = 1×10^4
794
796
798
800
7480
7490
7500
7510
Map View

**Figure 5.**

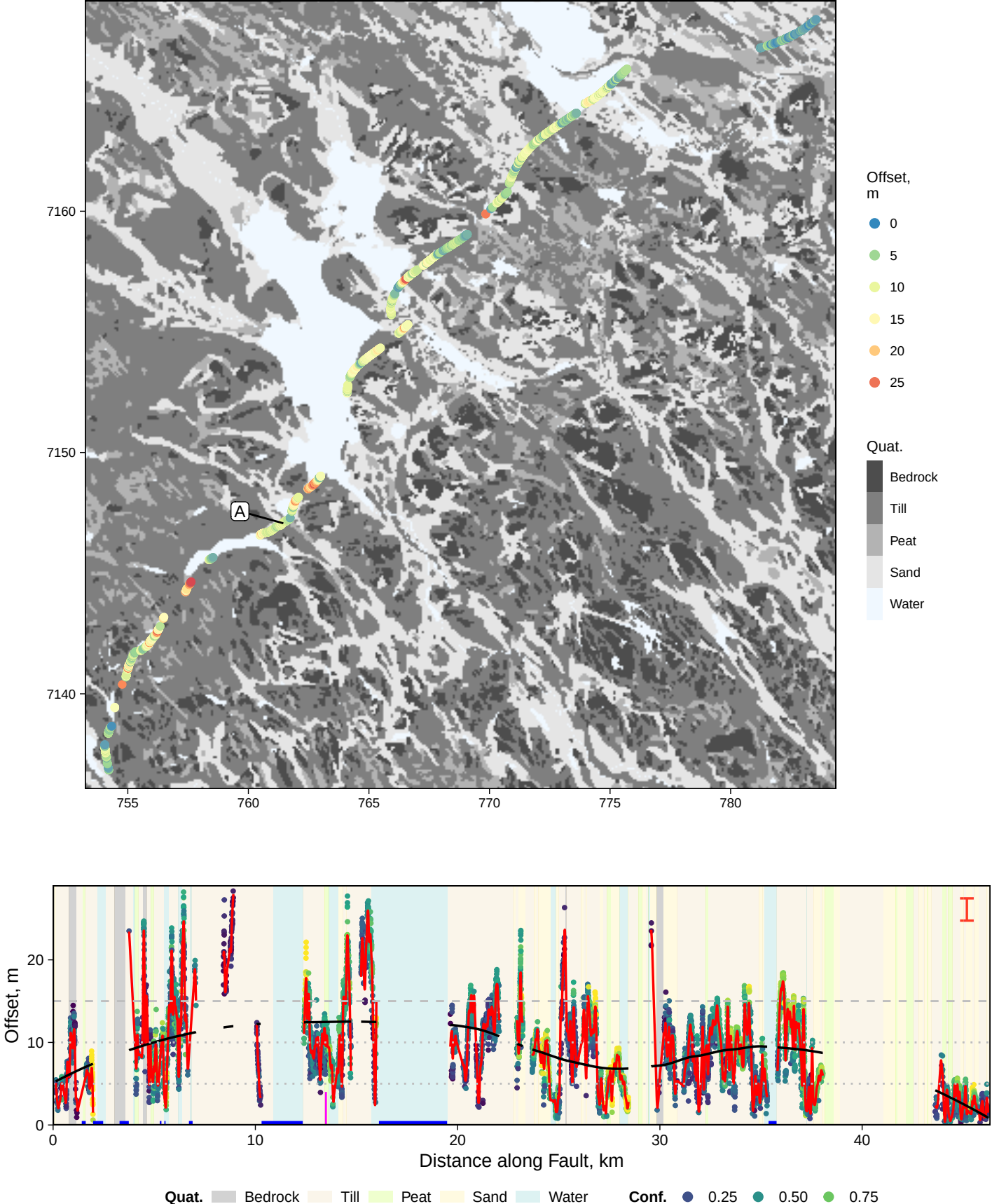
7160
7150
7140
755
760
765
770
775
780
A
Offset, m
0
5
10
15
20
25
Quat.
Bedrock
Till
Peat
Sand
Water
Offset, m
0
10
20
0
10
20
30
40
Distance along Fault, km
Quat. Bedrock Till Peat Sand Water
Conf. 0.25 0.50 0.75

**Figure 6.**

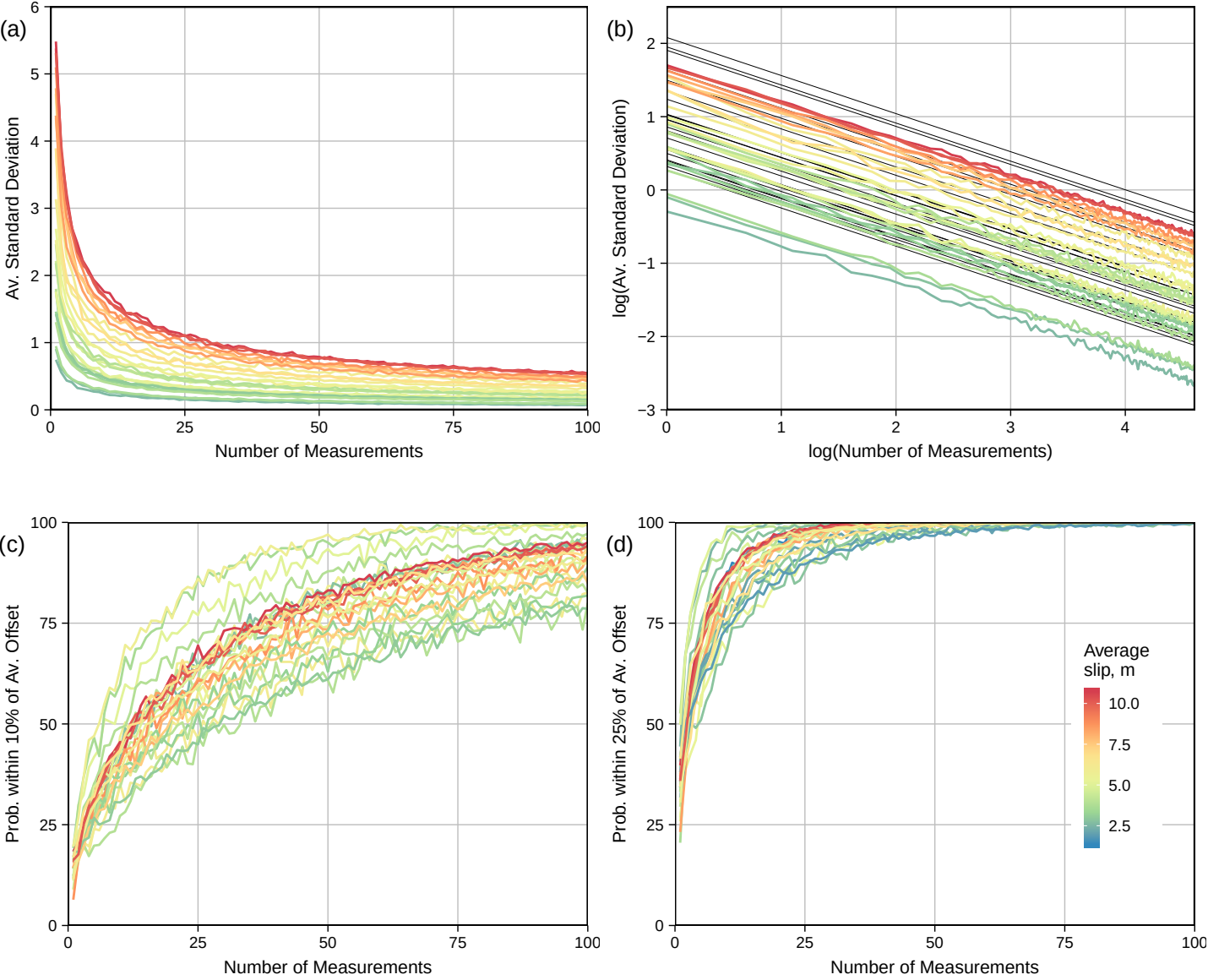
(a)
Av. Standard Deviation
Number of Measurements
(b)
log(Av. Standard Deviation)
log(Number of Measurements)
(c)
Prob. within 10% of Av. Offset
Number of Measurements
(d)
Prob. within 25% of Av. Offset
Number of Measurements
Average slip, m
10.0
7.5
5.0
2.5

**Figure 7.**

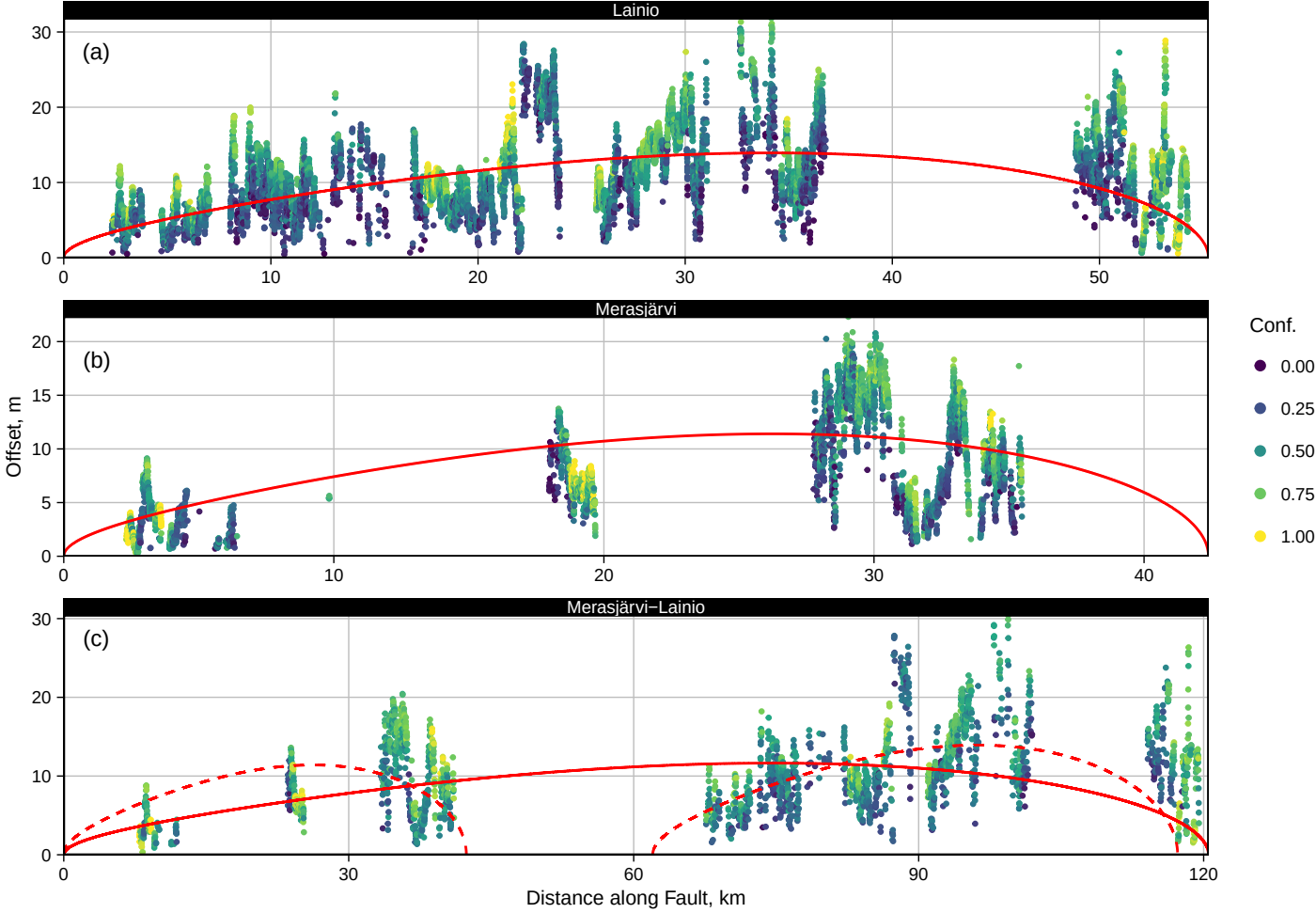
Lainio
(a)
Merasjärvi
(b)
Merasjärvi−Lainio
(c)
Offset, m
Distance along Fault, km
Conf.
0.00
0.25
0.50
0.75
1.00

**Figure 8.**

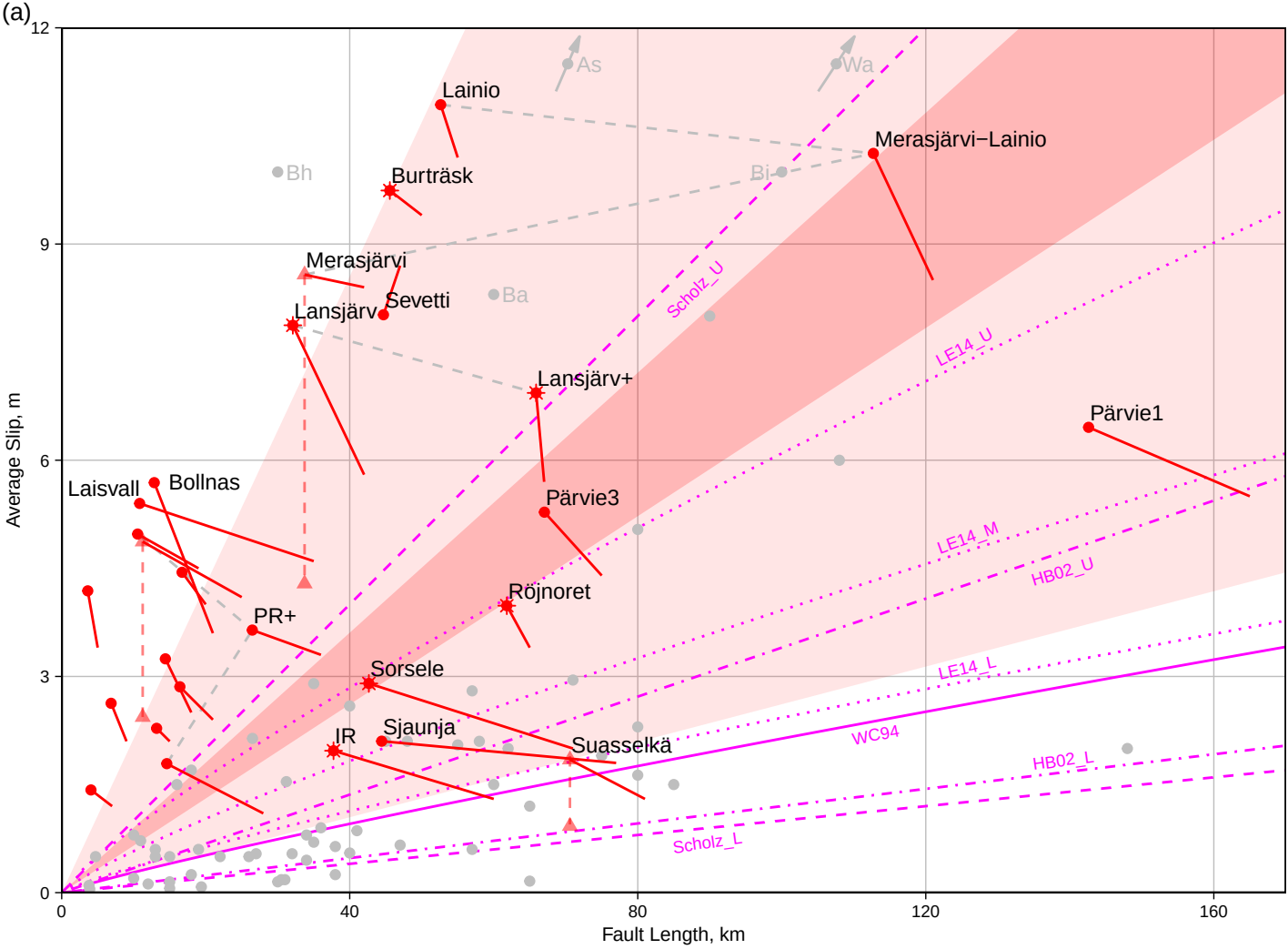
(a)
Average Slip, m
Fault Length, km
0
3
6
9
12
0
40
80
120
160
As
Wa
Bh
Bi
Ba
Lainio
Merasjärvi−Lainio
Burträsk
Merasjärvi
Sevetti
Lansjärv
Lansjärv+
Pärvie1
Laisvall
Bollnas
Pärvie3
Röjnoret
PR+
Sorsele
IR
Sjaunja
Suasselkä
Scholz_U
LE14_U
LE14_M
HB02_U
LE14_L
WC94
HB02_L
Scholz_L

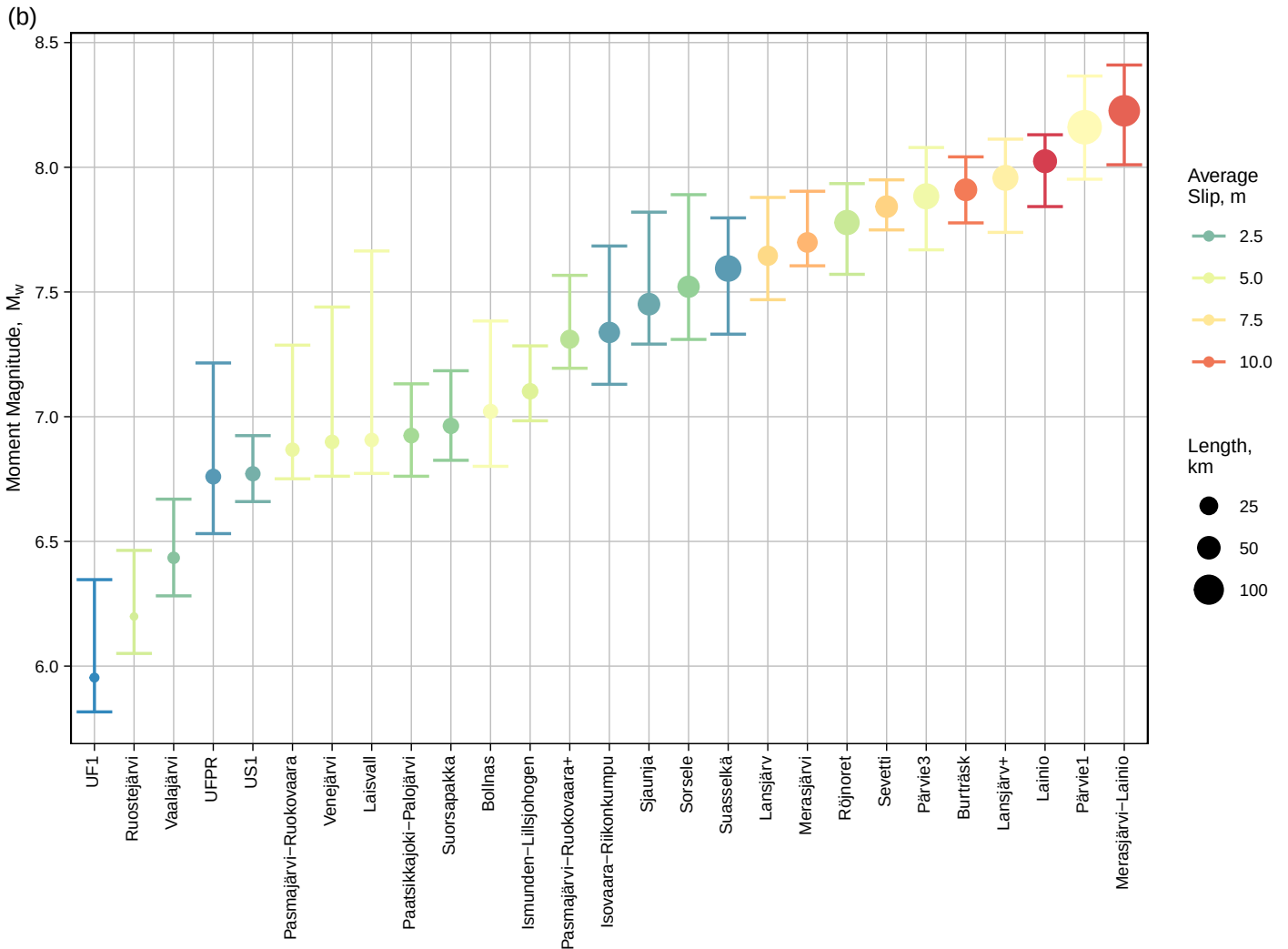
(b)
Moment Magnitude, $M_w$
6.0
6.5
7.0
7.5
8.0
8.5
UF1
Ruostejärvi
Vaalajärvi
UFPR
US1
Pasmajärvi−Ruokovaara
Venejärvi
Laisvall
Paatsikkajoki−Palojärvi
Suorsapakka
Bollnas
Ismunden−Lillsjohogen
Pasmajärvi−Ruokovaara+
Isovaara−Riikonkumpu
Sjaunja
Sorsele
Suasselkä
Lansjärv
Merasjärvi
Röjnoret
Sevetti
Pärvie3
Burträsk
Lansjärv+
Lainio
Pärvie1
Merasjärvi−Lainio
Average Slip, m
2.5
5.0
7.5
10.0
Length, km
25
50
100